Author Accepted Manuscript: Journal of Structural Geology, 2020

Dry, damp, or drenched? The effect of water saturation on the frictional properties of clay fault gouges

Steven Beynon*, Daniel Faulkner

Department of Earth, Ocean and Ecological Sciences, University of Liverpool, Jane Herdman Building, 4 Brownlow Street, Liverpool, Merseyside, L69 3GP, UK.

steven.beynon@liverpool.ac.uk

Abstract

Clay minerals often constitute a significant proportion of fault cores, yet the physics of clay friction, in particular the effect of free and interstitial bound (interlayer) water, is poorly understood. In this study, laboratory experiments were conducted on synthetic gouges under carefully controlled saturation states. Samples were sheared at room temperature under triaxial pressure at the following conditions: water saturated; room humidity; thermally dried and at room humidity; in a vacuum at room humidity; thermally dried and in a vacuum; in a vacuum and thermally dried within the pressure vessel. Friction coefficient (μ) is shown to increase with 'dryness' by a factor of 3 in 2:1 smectite and a factor of 2 in 1:1 sheet silicate, with largest increases in thermally dried samples. Analysis of constitutive frictional parameters (a-b) show that gouges become less velocity-strengthening with 'dryness'. The amount of displacement or time required to establish a new steady state μ upon a change in sliding velocity (d_c) decreases markedly in drier samples. Results suggest that the presence of water is key in promoting time and slip dependent frictional changes, constraining operative grain-scale deformation mechanisms to those that are fluid assisted. They also highlight the optimum laboratory procedures to investigate the frictional properties of clay-bearing materials.

Keywords: clay; friction; rate and state; saturation; fault gouge; triaxial

1. Introduction

The purpose of this paper is to investigate the contribution of water bound to phyllosilicates on their frictional behaviour. Understanding this behaviour is fundamental to constraining the larger scale behaviour of fault zones, informing models of fault strength and stability in geothermal reservoirs, carbon storage sites, and geological repositories of radioactive waste. Within upper crustal fault cores, fault gouge develops by a combination of mechanical attrition of the fault wall and authigenic crystallisation (Rutter and Maddock, 1987). Phyllosilicates are commonly abundant within this gouge (Sánchez-Roa et al., 2016). With a crystallographic structure capable of retaining large amounts of water (Schleicher et al., 2012), they may significantly influence fluid-assisted healing mechanisms, e.g. by forming planes of weakness with increased mobility and increasing the rate of pressure solution compaction (Bos and Spiers, 2000; Bos et al., 2000; Schleicher et al., 2013). In the laboratory, clay-rich fault gouges are consistently shown to be frictionally weak (Byerlee, 1978; Rutter and Maddock, 1987; Ikari et al., 2009a). In the field, the presence of clays has been inferred as a major reason for overall mechanical weakness of faults on scales over several orders of magnitude, such as subduction megathrusts (Saffer and Marone, 2003; Underwood, 2007; Den Hartog, 2013) and large strike-slip faults (Faulkner et al., 2008; Tembe et al., 2009; Lockner et al., 2011).

Clay contents in the fault core as low as 15-20% can significantly reduce fault strength (Shimamoto and Logan, 1981; Collettini et al., 2009). With depth, increasing pressures and temperatures in fault zones alters clay minerals in terms of dehydration, consolidation and mineralogy, thereby changing the fault's mechanical and seismic properties (Saffer and Marone, 2003; Sánchez-Roa et al., 2016; 2018). Dehydration in layered phyllosilicates is expected to occur with increased temperature and crustal depth (Bird, 1984). A decrease in water content may occur as a result of the loss of free and interstitial bound (interlayer) water (Morrow et al. 2000; Sánchez-Roa et al., 2018; Vidal and Dubacq, 2009). Dehydration may also occur by removal of water from hydroxyl (OH) groups within the crystal structure, thereby changing the hydration state, however this is not considered to be an important factor at the temperatures used for thermal dehydration in this study. Where the number of phyllosilicate-bound water layers is fixed, dehydration occurs by slight continuous loss of the interlayer water (associated with most volume decrease) after initial rapid removal of free water (<~0-120 °C). Larger, discontinuous losses of water layers and comparatively minor volume decreases also occur upon progressive collapse of the interlayer space (>~120 °C) (Bala et al., 2000; Vidal and Dubacq, 2009). Smectites (swelling clays) are increasingly recognised as 'problem minerals' in geothermal reservoirs due to their prevalence in fractures, with low permeability creating barriers to fluid flow (Vidal et al., 2018). The presence, and more specifically dehydration, of smectites is considered to be an important factor in controlling the propagation of subduction zone earthquakes and the limits of seismicity (e.g. Faulkner et al., 2011; Morrow et al. 2000; Saffer & Marone, 2003; Takahashi et al., 2009), and has also been shown to contribute to land subsidence and sediment overpressuring (Bethke, 1986).

Many authors have attempted to explain the fact that phyllosilicates seemingly do not adhere to Byerlee's law of static friction coefficients (μ) (Byerlee, 1978), where $0.6 \leq \mu \leq 0.85$ (e.g. Ikari et al., 2007, 2009, Moore & Lockner, 2004, 2007; Morrow et al., 1992; Morrow et al., 2000, 2017; Saffer & Marone, 2003). The upper limit of μ in clays is often found in laboratory experiments to be much lower than expected (e.g. $0.03<\mu<0.50$ for montmorillonite, chlorite and illite (Ikari et al., 2009a)). Whilst a positive correlation of μ with effective normal stress, said to be characteristic of sheet-silicate gouges, has been described in montmorillonite

(Moore and Lockner, 2007), μ has also been shown to decrease (and shear strength increase), with effective normal stress in smectite and illite (Saffer et al., 2001; Saffer and Marone, 2003; Ikari et al., 2007). Frictional weakening has often been attributed to lubrication of clay grains by thin films of adsorbed water (aqueous pore fluid), which may be expelled by increased effective normal stress (Israelachvili et al., 1988) thereby increasing μ (Moore and Lockner, 2007), or to sub-critical delamination of phyllosilicates (Den Hartog et al., in press). Due to their low permeability, the effect of increasing pore-fluid pressure may be magnified in clay-rich fault gouges, reducing effective stress and fault strength and promoting failure (Morrow et al., 1992; Faulkner and Rutter, 2001; Frye and Marone, 2002; Noda and Shimamoto, 2005; Faulkner et al., 2018). Dry friction coefficients of clays measured in the laboratory are assumed to be the upper limit of strength at depth on a given fault, since increases in pressure are likely to remove water films from platy surfaces and increase shear strength (Israelachvili et al., 1988; Renard and Ortoleva, 1997).

Published data on individual clay frictional properties is variable; such variability may result from differences in room humidity and/or sample saturation state, which is usually not well-defined or controlled (Reinen et al., 1994; Frye and Marone, 2002; Moore and Lockner, 2004; Ikari et al., 2007, 2009a; Morrow et al., 2017; Tetsuka et al., 2018). No truly dry reference condition for phyllosilicates has yet been established, and many fall into the ‘partially saturated’ region of Figure 6 in Morrow et al. (2017), despite initially being referred to as ‘dry’. Montmorillonite, for example, has yielded μ values between 0.06 and 0.78 in tests conducted under supposedly similar conditions in different laboratories, which has been attributed to different deformation processes occurring under different relative saturation states (Moore and Lockner, 2007; Morrow et al., 2017). The correlation between dry friction coefficient and interlayer (001) bonding energy (ILBE) (Giese, 1978, 1979; Moore and

Lockner, 2004) is debated partly because of the disparity in test conditions used to obtain μ values, such as variations in the applied stress and non-comparable controls on the distribution of grain size and shape (Behnsen and Faulkner, 2012; Sakuma and Suehara, 2015).

The relationship between sliding friction, displacement and displacement rate can be described by constitutive relationships of rate- and state-dependent parameters (Dieterich, 1972, 1978, 1979; Ruina, 1983; Blanpied et al., 1998; Marone, 1998). Although modelling of these parameters has been successfully applied to many datasets in order to understand the stability of frictional sliding, the micro-scale physiochemical mechanisms responsible for behaviours they describe are poorly understood. Upon a change in displacement rate, an initial direct effect occurs where μ is scaled by a constant 'a' (Figure 1). μ then exponentially evolves over a characteristic distance, 'd_c', which is considered to relate to gouge layer thickness, normal stress, surface roughness and particle size (Biegel et al., 1989; Li et al., 2011; Linker & Dieterich, 1992; Marone, 1998; Marone and Kilgore, 1993). Effective contact time evolves during shear, and is derived from the ratio of d_c to the slip velocity (Dieterich, 1979; Mair and Marone, 1999). The magnitude of the change is scaled by a constant 'b'; this 'state' effect is a proxy for the quality and/or area of asperities in contact across the sliding interface. These variables are related by two coupled equations – the friction law, and either the Aging (time-dependent) Law (Dieterich, 1978) or the Slip Law (Ruina, 1983). The friction coefficient is a function of the current sliding velocity (rate), and the state variable can be thought of as a memory of past sliding (Ruina, 1983). State evolution in terms of time or slip remains a matter of debate (Bhattacharya et al., 2017). The Slip Law implies that any frictional change requires slip, whereas Dieterich's law implies that state and friction evolve purely as a function of time if frictional surfaces are in contact, even with zero velocity. Once sliding is initiated, frictional resistance transiently adjusts to a new steady state. Since deformation mechanisms may differ between dry and saturated sheet silicate gouges, the velocity dependence of dry and saturated shear strengths may also differ (Moore and Lockner, 2004).

Rate dependence can be important in determining whether deformation is stable or unstable (Lockner et al., 2011). At low effective pressures (12-60 MPa) and displacement rates between 0.5-300 μms^{-1}, clay-rich gouges typically display stable fault creep and velocity-strengthening behaviour, such that (a-b)>0 (Figure 1) (Logan and Rauenzahn, 1987; Morrow et al., 1992; Scholz, 1998; Ikari et al., 2007, 2009a, 2011). The constants a and b (Figure 1) are ≈0.01 (Bhattacharya et al., 2017), but may vary by an order of magnitude with changing temperature and humidity (Blanpied et al., 1998). For example, alumina gouge has been shown to transition from velocity-strengthening to velocity-weakening behaviour at ~55-60% room humidity (Frye and Marone, 2002). Whilst smectites are usually velocity-strengthening (e.g. Ikari et al., 2009a), slight velocity-weakening behaviour has been observed under specific conditions, such as at low normal stresses and higher displacement rates (Saffer et al., 2001; Saffer and Marone, 2003).

In response to the uncertainty in the role of water in determining frictional properties highlighted by previous studies, this study explores how friction coefficient and the constitutive parameters of frictional stability, a, b and d_c (Figure 1) behave in relation to the amount of free and hydrogen-bound water in kaolinite and Mg-montmorillonite samples in carefully controlled laboratory experiments. It is hoped that this work will help to understand the effect of different saturation states on micromechanical processes that are responsible for phyllosilicate friction, as well as how laboratory studies can effectively investigate this.

2. Methodology

A total of 18 triaxial direct shear experiments were performed to determine the frictional strength and constitutive parameters on 2 clays under different saturation states. 6 experiments were carried out on kaolinite-rich china clay, each with a repeat run, and 6 on Mg-montmorillonite. Repeat runs were not performed on montmorillonite due to a limited amount of material. Each experiment included three velocity steps. Tests were run under the following experimental conditions for each gouge sample, at a confining pressure (P_c) of 60 MPa unless otherwise indicated. Where heat was applied, 130 ˚C was chosen as a temperature that was high enough to remove free and interstitial bound water from the clays, but lower than that required to promote structural changes (e.g. OH structural water layers strongly coordinated to the interlayer cations; dehydroxylation) (Takahashi et al., 2009; Bala et al., 2000).

1. "Saturated": Samples were prepared at room humidity (50-60 %), and sheared with 80 MPa P_c and 20 MPa deionised water fluid pressure (P_f) applied;
2. "Room Dry": Samples were prepared at room humidity (50-60 %), transferred to the pressure vessel, and sheared at room humidity after ensuring the sample assembly and pore fluid pipework was thoroughly dry;
3. "Room Dry + Vacuum": Samples were prepared at room humidity (50-60 %), transferred to the pressure vessel, and sheared with a vacuum applied to the pore-fluid inputs of the thoroughly dry sample assembly to prevent humidity changes during the experiment;
4. "Oven Dry": Samples were prepared at room humidity (50-60 %) before being dried in a vacuum oven at 130 ˚C for 20 hours and cooled to room temperature under vacuum. Samples were transferred to the pressure vessel and sheared at room humidity after ensuring the sample assembly and pore fluid pipework was thoroughly dry;
5. "Oven Dry + Vacuum": Samples were prepared at room humidity (50-60 %) before being dried in a vacuum oven at 130 ˚C for 20 hours and cooled to room temperature under vacuum.

Samples were transferred to the pressure vessel and sheared with a vacuum applied to the pore-fluid inputs of the thoroughly dry sample assembly to prevent humidity changes during the experiment;

6. “Heat + Vacuum in Vessel”: Samples were prepared at room humidity (50-60 %) and transferred to the pressure vessel, where they were heated under vacuum in the thoroughly dry sample assembly to 130 ˚C for ~20 hours and allowed to cool to room temperature whilst still under vacuum. Samples were then sheared under vacuum.

2.1 Phyllosilicate Gouge Sample Properties

Gouges explored in this study are kaolinite-rich gouge and Mg-montmorillonite gouge. These clays were chosen specifically to investigate the effect of dehydration on frictional properties in swelling versus non-swelling clays. The kaolinite-rich china clay sample had a grain-size fraction of <2μm and comprised 75% kaolinite, 14% illite/muscovite, 8% K-feldspar and 3% quartz (analysed by X-ray diffraction - XRD). The Mg-montmorillonite sample used was the same as described in Behnsen & Faulkner (2013), derived from Wyoming bentonite (obtained from RS Minerals). This sample, shown by XRD to contain >98% montmorillonite, was separated by centrifugation and also contained only the <2 μm grain-size fraction. The principal cation was exchanged for Mg using the methodology described in Behnsen and Faulkner (2013). The amount of water adsorbed onto clay surfaces strongly correlates with the mineral’s specific surface area (SSA) (Diamond and Kinter, 1958; Moore and Lockner, 2007). Montmorillonite has a SSA of ~600-800 m^2/g for the grain size fraction used in this study (<2 μm), mostly located within its interlayer surfaces, which enables it to hold more water than kaolinite and illite, with SSAs of ~7-30 m^2/g and 67-100 m^2/g respectively (Diamond and Kinter, 1958).

Phyllosilicates are characterised by stacked platy crystals of one or more silicate tetrahedral (T) layers and a hydroxyl (OH) and Al-/Mg-based octahedral (O) layer (Behnsen and Faulkner, 2012; Lázaro, 2015) (Figure 2). Both kaolinite and montmorillonite are common low temperature alteration minerals, usually formed by low temperature hydrothermal breakdown of feldspar and volcanic glass respectively (Lázaro, 2015; Inoue and Utada, 1988). Kaolinite ($Al_2Si_2O_5(OH)_4$) is a dioctahedral 1:1 sheet silicate, where T-O sheets are bonded to the adjacent sheet via long hydrogen-oxygen bonds. Sheets have a basal spacing of 0.7 nm, are charge-balanced, and the bonds that hold successive layers together are relatively weak (Lázaro, 2015). Free water molecules may be bonded to the external layers of kaolinite T-O sheets. Montmorillonite ($Ca_{0.16}(Mg_{2.67}Al_{0.33})(Si_{3.34}Al_{0.66})O_{10}(OH)_2.nH_2O$) (Moore and Reynolds, 1997) is a dioctahedral smectite variety of a 2:1 sheet silicate, where each layer comprises an octahedral sheet between two tetrahedral sheets (T-O-T). Chemical substitutions in the sheets, which have a basal spacing of ~1 to ~1.5 nm, result in a residual layer charge, and sheets are separated by cations (in this case Mg) for charge balance (Karnland et al., 2016; Lázaro, 2015). In naturally occurring montmorillonite, cations may be a mix of Na^+, Ca^{2+}, K^+ and Mg^{2+}. Unlike kaolinite, montmorillonite is a swelling clay in which dipolar water may be bonded to both external crystal surfaces *and* the interlayer cations. Depending on the cation type, which have different bonding energies, significant quantities of water (with a thickness of up to 4 nm) may be bound by the interlayer cation (Behnsen and Faulkner, 2013; Karnland et al., 2016; Moore and Lockner, 2007; Morrow et al., 2017; Vidal and Dubacq, 2009). Cation substitution and associated water uptake/removal occurs relatively easily with changes in temperature, pressure and fluid chemistry (Schleicher et al., 2013). Mg-Montmorillonite is chemically and structurally similar to the Mg-rich trioctahedral smectite saponite (Inoue and Utada, 1988; Karnland et al., 2016), which has been inferred to be the principal cause of frictionally weak sections of the San Andreas Fault Zone from the SAFOD core (Carpenter et al., 2012; Holdsworth et al., 2011; Lockner et al., 2011).

2.2 Sample Preparation

For both clay types, 1.2 g of powdered clay gouge (size fraction <2 µm) was placed into a stainless-steel direct shear assembly (Figure 3a), with a contact surface area of 720 mm^2. To prevent sample loss during preparation, this was pre-compacted with a hand lever press into a uniformly ~1 mm thick wafer with a 5 MPa normal stress. Saturated, room humidity and room humidity vacuum experiments were prepared in a laboratory relative humidity of ~55-60 %.

For experiments run with oven dry samples, compacted gouge was placed together with the slider assembly (without the PVC jacket) into a vacuum oven at ~130 ˚C for ~20 hours. The combination of time and temperature was considered to be sufficient to remove any adsorbed water from the clays based on data published in Mackenzie, (1957), Carpenter et al. (2016), Ikari et al. (2007) and Morrow et al. (2017), and was also supported in this study with thermogravimetric analysis (Section 2.3.1). Prior to testing, samples were allowed to cool to room temperature whilst still under vacuum.

After heating (if applicable), metal sliders were wrapped in PTFE film (in order to reduce friction between sliders and jacket). The slider assembly was inserted into a PVC jacket in all experiments besides those heated within the vessel (see later), in which case a more heat-resistant viton (fluoroelastomer) tubing was used. PVC jackets have been shown to be sufficiently weak so as not to contribute significant error to clay friction measurements (Behnsen and Faulkner, 2012); differences between PVC and viton tubing was not tested in this study but are assumed to be comparable. The setup above was then immediately inserted into a sample assembly as shown in Figure 3a (and described in Faulkner et al., 2018), and placed into a triaxial deformation apparatus. Total preparation time, which could be crucial in oven dried samples as they may be rapidly contaminated with room humidity, was never longer than ~10-15 minutes.

2.3 Experimental Procedure

2.3.1 Analysis of absolute water content

In order to measure relative water loss between room dry samples (experiment type 2) and those that were heated (experiment types 4-6), two methods were employed: 1. Direct mass difference before and after heating to 130 °C; 2: Thermogravimetric Analysis (TGA). Relative room humidity was on average ~50-60 %.

In direct mass difference measurements, the 1.2 g gouge sample and the 65.0 g metal sliders were weighed separately immediately before and after heating in a vacuum oven at 130 °C. Relative mass loss was recorded as a percentage of total mass difference, separately and combined for the sample and metal sliders. The difference between the two sample measurements is regarded as the water loss from the sample in wt% between conditions in experiment type 2 (“room dry”) and experiment type 4 (“oven dry”). The gouge sample and metal sliders were also weighed after being removed from the vacuum oven. This was done immediately, and at intervals of 5, 10, 15 and 30 minutes in order to observe the effect of time spent at room humidity on water reabsorption in the sample. The difference between values obtained ‘immediately’ and after 15 minutes was interpreted to reflect water loss between experiment type 2 (“room dry”) and experiment type 5 (“oven dry + vacuum”), representing the typical time taken to transfer the sample from the oven to the assembly and pressure vessel before applying a vacuum.

TGA analyses were carried out using a Netzsch Simultaneous Thermogravimetric Analysis (STA) 449 F1 Jupiter analyser using a sapphire (Al_2O_3) disk as a reference standard. TGA measures the change in sample mass during heating under vacuum, which is interpreted to indicate volatile release. The difference between the initial mass and final mass is regarded as the water loss from the sample in wt% between conditions in experiment type 2 (“room dry”) and experiment type 6 (“heat + vacuum in vessel”), since in the latter experiment the sample was not exposed to room humidity conditions at any point during preparation or testing.

2.3.2 Friction Tests

Experimental conditions were chosen to represent various methods for removing water films from clay grain surfaces. All tests were performed in a triaxial deformation apparatus in the University of Liverpool’s Rock Deformation Laboratory (as in Faulkner & Armitage, 2013). All mechanical loading was carried out at room temperature (~22 °C) and at 60 MPa effective pressure (P_{eff}) (where $P_{eff} = P_c - P_f$). For saturated experiments, confining pressure was carefully applied at a rate of ~0.1 $MPas^{-1}$. ensuring that the sample was thoroughly saturated before compacting, yet without inducing overpressure and fluidising the gouge.

The pore fluid used was deionised water, which was introduced to the upstream and downstream ends of the metal sliders (Figure 3a). Pore pressure was introduced at a rate of ~0.05 $MPas^{-1}$ and left to equilibrate for up to ~20 hours. Equilibration times were calculated based on diffusion modelling (for details see Supplementary Material). Fluid was allowed to infiltrate the sample via three porous sintered disks normal to the sample on each side, resulting in an even distribution of fluid pressure across the gouge wafer. A steady fluid pressure and pore fluid volume before and during experiments was taken as an indicator that the sample was fully saturated and adequately drained.

The surfaces of the stainless-steel sliders are grooved in order to prevent shear localisation at the slider-sample interface. Initial contact area between the slider surface and the sample was 720mm^2. Samples were sheared to 6.25mm displacement by applying a constant axial piston driving rate, resulting in a final contact area of ~845mm^2. An area correction was not applied to the data throughout the experiment (which would result in final μ being ~8-10 % lower than reported here), since areas overlapping non-grooved areas of the metal sliders, filled by very low strength silicon rubber spacers (Sanchez-Roa et al., 2017), do not significantly contribute to frictional strength. Displacement rates were varied so as to investigate rate and state friction properties, with a run-in at 0.3 μms^{-1} for 2.5 mm to allow the development of a steady state shear strength (Faulkner et al., 2018), followed by three velocity steps to 3 μms^{-1} and back down again every 0.5 mm.

2.3.3 Vacuum Setup and Use

Care was taken to ensure that the vacuum applied to the sample assembly was present and quantified at all times during experiments. In order to do this, the pore fluid system was configured as in Figure 3b. The vacuum level was initially tested with minimal capillary tubing and connections, and without connecting it to the sample assembly, in order to test the best achievable vacuum level. Further tests were then carried out with the sample assembly connected using a blank sample. A comparable vacuum level was achieved in each of these tests, indicating the system is capable of being sufficiently sealed. 0.04±0.1 mbar was the best vacuum level achieved, varying to 0.13±0.1 mbar in some tests.

A suitable level of vacuum was achieved within a few minutes with a blank sample in place. With clay gouge samples, however, the time taken to achieve a vacuum is affected by the porosity and permeability of the sample and metal sliders, the thickness of the gouge sample, mean free path of air molecules, air viscosity at room temperature, and air compressibility. Fluid diffusion modelling outputs indicate that for kaolinite, an equilibration time of ~40 minutes is sufficient to achieve a vacuum throughout the sample (Supplementary Figure 1). For montmorillonite, which has a lower starting porosity and permeability (Behnsen and Faulkner, 2013), an equilibration time of ~4 hours is more applicable. Samples were left under vacuum overnight prior to each vacuum test (~15 hours).

2.3.4 Scanning Electron Microscopy

A range of sheared samples were selected for microstructural analysis under the scanning electron microscope (SEM), aimed at representing a transition from the wettest to driest sheared gouge. Microstructures are assumed to represent deformation processes occurring in the final velocity step. Gouge wafers were carefully removed from the slider setup, air-dried at ~25 °C, and impregnated with epoxy resin under a vacuum. It was noted that, in particular in dry montmorillonite samples, the wafers quickly began to fall apart once exposed to room humidity, which rendered some unsuitable for SEM analysis. Difficulties in preparing montmorillonite in epoxy also arose from the extremely low permeability of the samples. Due to a combination of these factors, only kaolinite microstructures are considered in this study.

Once dry, blocks were cut perpendicular to the sliding surface and parallel to the shear direction, turned 90 degrees and re-impregnated with the same epoxy resin. Sample blocks were then polished using aluminium oxide powder (to 0.03 µm grain size) and carbon coated. The internal microstructure of each gouge wafer was analysed on a Philips SEM.

2.4 Data Analysis

2.4.1 Friction Coefficient

The coefficient of sliding friction (μ) was calculated for each datapoint (recorded at 2 Hz) from the measured shear stress and normal stress by applying the following equation:

$$\mu = \tau / \sigma'_n \qquad \textit{(Eq. 1)}$$

(Byerlee, 1978), where τ is shear stress and σ'_n is the effective normal stress (in this case confining pressure minus pore pressure).

There is no convention for defining when during an experiment friction coefficient should be defined, partly due to the fact that different samples reach a steady-state microstructure before others (which is difficult to determine). This has resulted in some confusion within the literature as to how comparable studies between different authors and laboratories may be. In this study, steady state μ is taken as the value reached after ~2.5 mm of displacement, immediately prior to the first displacement velocity jump. In all experiments, μ at this point has minimal variation and approximately represents the mean value after the yield point. μ at yield point is defined as the intersection between two lines of best fit drawn 1. through the loading stage, and 2. through the steady state sliding stage following yield.

2.4.2 Rate and State Friction Modelling

The frictional stability was calculated using the friction state parameter a-b, as derived by Dieterich (1978, 1981) from the constitutive law describing rate- and state-dependent friction.

This relationship is schematically illustrated in Figure 1 for a) velocity-strengthening and b) velocity-weakening behaviour, where a-b values are positive and negative respectively.

Rate and state parameters were determined from velocity up-steps using a non-linear least-squares fitting routine with the machine stiffness treated as a fitting parameter (Noda and Shimamoto, 2009). d_c may either be a product of time or slip distance (Dieterich, 1979; Ruina, 1983). The constitutive law used for modelling was the Aging Law (Dieterich, 1978; Marone, 1998; Bhattacharya et al., 2017), for which standard deviations are up to 8 times smaller than the Slip Law. Data were fit by a single set of state variables (a, b, d_c) with a linear detrend.

3. Results

3.1 Analysis of Absolute Water Content

Mass loss during thermal sample preparation was measured using an electronic balance immediately before and after being vacuum oven dried at 130 °C for 20 hours. This is interpreted to represent water loss between conditions in experiment type 2 (“room humidity”) and experiment type 4 (“oven dry”). From three samples, this method yielded average mass losses during heating of 0.53 wt% (absolute loss 0.006 g) in kaolinite and 7.95 wt% (absolute loss 0.060 g) in Mg-montmorillonite (Figure 4), implying negligible and considerable water loss respectively. Metal sliders dried from room humidity also showed evidence of considerable water loss, decreasing in mass during heating by 0.26±0.09 g (0.40±0.14 wt%). After 5 minutes, regained mass due to water reabsorption reduced the relative mass loss in kaolinite to, on average, 0.16 wt% and 5.15 wt% in Mg-montmorillonite (Figure 4). After 10, 15 and 30 minutes, relative mass loss values in kaolinite remained fairly consistent at 0.26, 0.26 and 0.10 wt% respectively; in Mg-montmorillonite, relative mass loss values decreased to 4.96, 4.49 and 2.23 wt% respectively. Mass loss after ~15 minutes is interpreted to represent water loss between conditions in experiment type 2 (“room humidity”) and experiment type 5 (“oven dry + vacuum”).

Relative water loss in kaolinite from room humidity samples heated to and held at 130 ˚C, as measured via STA, was ~0.3 % for kaolinite and ~4.5 % for Mg-montmorillonite (Figure 4). This is interpreted to represent water loss between conditions in experiment type 2 (“room humidity”) and experiment type 6 (“heat + vacuum in vessel”). In both sample types, most mass loss occurred during the first hour of heating (50-130 ˚C). Mg-montmorillonite continued to lose some mass during the 6-hour 130 ˚C hold period, whereas kaolinite did not. An increase in temperature to 200 ˚C at the end of the test produced a further ~0.4 % mass loss in Mg-montmorillonite but had no effect in kaolinite.

3.2 Friction Coefficient

Friction coefficient data is summarised in Table 1 and Figures 5 & 6. When fully saturated, kaolinite gouge (Figure 5a) has an initial yield strength peak of 0.27 and reaches a slightly lower steady state at 0.25. Values for ‘dry’ kaolinite vary considerably, with yield strengths ranging from 0.28 to 0.4, and steady state values ranging from 0.29 to 0.49, resulting in an overall rounder yield curve than that of saturated samples.

Fully saturated Mg-montmorillonite gouge (Figure 5b) is weaker, with a peak yield strength of 0.16 and a lower steady state of 0.12. ‘Dry’ values vary to a much greater extent than those of kaolinite, with yield strengths ranging from 0.17 to 0.58, and steady state values ranging from 0.19 to 0.57. Samples that have been subject to thermal drying during preparation, however, consistently display μ values of ~0.57. Plot shapes for ‘dry’ Mg-montmorillonite are also rounder at yield point, but not to the same extent as those for kaolinite.

Repeatability of the experimental dataset is illustrated by the range of kaolinite data in Table 1 and Figure 6. For all experiments except those at room humidity, repeatability for kaolinite was excellent for both yield and steady state μ, with a maximum variation of ~0.025 during an identical experiment. For experiments at room humidity, data were much more variable, with μ for kaolinite ranging between ~0.3 and ~0.4. This variation is likely due to differences in absolute water content within the sample caused by minor fluctuations in room humidity. μ for saturated Mg-montmorillonite in this study (0.12) is comparable to that measured on the same sample in Behnsen & Faulkner (2013) (0.11), hence despite tests not being repeated, results for montmorillonite are not expected to vary greatly.

The difference between yield strength and steady state friction coefficient is also highlighted in Figure 6. With increasing confidence of 'dryness', yield strength becomes progressively lower than steady state strength. For example, in room humidity kaolinite, yield strength is 0.01 to 0.03 lower than steady state friction coefficient, whereas in the sample tested under vacuum after being heated in the vessel, yield strength is 0.09 to 0.13 lower than steady state. In fully saturated samples, yield strength is consistently slightly higher than steady state friction coefficient. Steady state conditions are reached in most samples after ~1.5-2 mm of displacement, prior to the 2.5 mm point used to obtain this reading.

3.3 Rate and State Parameters

Rate and state friction data are summarised in Table S1 and Figure 7. Data from some experiments are not included in this analysis due to significant error in the modelling process, where standard deviation was greater than the total range of values across the dataset and hence deemed unreliable. Both kaolinite and Mg-montmorillonite display velocity-strengthening behaviour (a-b is positive) for all experiments (Figure 7a). For kaolinite, a-b values range from ~0.001 to ~0.006. The smallest a-b values for kaolinite are exhibited in all 'dry' samples, with considerable variation between different modelled velocity steps. For Mg-montmorillonite, a-b values range from ~0.003 to ~0.008. Again, the smallest a-b values for Mg-montmorillonite were exhibited in 'dry' samples, particularly in those that were thermally treated.

Values of a (Figure 7b) for kaolinite vary between ~0.001 to ~0.08, initially with a general trend towards lower values between saturated and drier samples, yet increasing in scatter between modelled velocity steps for the driest samples. For Mg-montmorillonite, a values vary between ~0.002 and ~0.09, with higher values in drier samples than in saturated. Values of b (Figure 7c) for kaolinite vary between ~-0.001 and ~0.08, with highest values in the driest samples and little difference between saturated and 'room dry' experiments. Driest experiments display considerable variation between different modelled velocity steps. For Mg-montmorillonite, b values vary between ~-0.001 and ~0.005, and also display an increase towards drier samples, particularly in those that have been heated.

Values of d_c (Figure 7d) for kaolinite vary between ~3 and ~50 microns, with a clear trend towards lower values in drier samples, with some variation between modelled velocity steps. For Mg-montmorillonite, d_c values vary between ~1 and ~100 microns. Lowest values are also in drier samples, yet here there is a marked decrease between similar values in non-thermally treated and thermally treated samples. There is no obvious correlation between each successive velocity step and value of a, b or d_c in either material.

3.4 Kaolinite Microstructure

SEM images of sheared kaolinite fault gouges, representing the microstructures developed during the final velocity step, display an evolution between saturated and vacuum + oven dry samples (Figure 8). Using the terminology of Rutter et al. (1986), saturated samples display two prominent Y boundary shears towards each edge of the sample (Figure 8a-c), with a lack of observable microstructures in between them. Where Riedel (R_1) and P shears are observed, they are generally poorly developed and rarely linked. Samples sheared at room humidity (Figure 8d-f) again have prominent Y shears, however these are more irregular than in saturated samples and often filled with small, angular 'clasts' of material. P shears are well developed through the sample where present, and are linked to R_1 shear crenulations, but again are rare. In samples prepared at room humidity and run under vacuum (Figure 8g-i), and those heated to 130 °C and cooled in the pressure vessel under vacuum (Figure 8j-l), the internal microstructure is markedly different to samples sheared at room humidity. Rather than shear localisation occurring on two Y shears, multiple Y and P foliations appear to accommodate deformation throughout the sample, with abundant R_1 and R' shears oblique to these.

4. Discussion

4.1 Evolution of Friction Coefficient with Saturation State

Experimental results presented here show increasing friction coefficient with removal of free and interlayer water in both kaolinite-rich china clay and Mg-montmorillonite. Factors such as water pH, pressure-temperature conditions, and grain size, shape, composition and distribution may all influence to some degree the amount of water that may be adsorbed by phyllosilicates and hence the friction coefficient (e.g. Behnsen and Faulkner, 2012; Morrow et al., 2000; Sakuma and Suehara, 2015), however all of these have been kept consistent for each material in all experiments. Published μ data for these minerals show considerable differences between different studies and laboratories, and the question we aim to address here is whether the level of 'dryness' of the experiments conducted (which is not always specified) can explain the differences reported in the literature.

Sheet minerals with thin films of interlayer water between them, such as montmorillonite, have a shear strength that increases as the number of layers decreases (Israelachvili et al., 1988) (Figure 2). The amount of free and interstitial bound water inferred to have been lost during vacuum drying of room dry samples at elevated temperatures in this study (Figure 4) is consistent with Morrow et al. (2017), (7.2-7.9 wt% water loss in montmorillonite), whilst Bird (1984), Ikari et al. (2007) and Carpenter et al. (2016) all reported a higher water loss of 11-16 wt%. The majority of free and interstitial bound water in Mg-montmorillonite removed upon heating to 130 °C (~4.5-9.5 %) occurs within the first hour, and >90 % of this is removed within 3 hours, which agrees with published time-dependent drying curves for Ca-montmorillonite (Ikari et al., 2007). An increase in temperature to ~200 °C from 130 °C resulted in a further ~0.4 wt% decrease in water in both STA and direct mass experiments (Figure 4), suggesting that some interstitial water was still present in the Mg-montmorillonite sample in experiment types 4, 5 and 6. Mg-smectites with three water layers have been shown to contain >~8 wt% water, whilst two water layer arrangements contain ~7–8 wt%, one water layer arrangements contain ~4–6 wt% and dry layers contain <~3 wt% water (Schleicher et al., 2013), although some higher values have been reported (e.g. Bird, 1984; Ikari et al., 2007). Colten-Bradley (1987) showed that whilst one water layer may be expelled from a two-layer montmorillonite at 67-80 °C, the remaining layer may still be present up to 192 °C. Indeed, dehydration does not necessarily have a clear end point and may continue beyond 200 °C (e.g. Bala et al., 2000). It is therefore important to state that whilst we can infer that a substantial amount of free and interstitial water has been removed from our samples, minor amounts of interstitial water may remain in the montmorillonite. Since the removal of a single water interlayer causes the largest frictional strength increase (Bird, 1984), the possibility that a small amount may remain in the sample at the temperatures used during preparation in this study will likely have negligible impact.

Assuming ambient temperature and room humidity are consistent between studies, and therefore that montmorillonite at room humidity contains interstitial bound water in a two-layer configuration (Bird, 1984), absolute differences in water contents at room humidity are likely strongly controlled by crystal structure, layer charge and cation type (Behnsen & Faulkner, 2012; Bird, 1984; Ikari et al., 2007; Karnland et al., 2016; Morrow et al, 2000; Sakuma and Suehara, 2015; Vidal and Dubacq, 2009). In ‘dry’ phyllosilicates, μ is often much larger than expected in relation to a suggested positive correlation with interlayer (001) bonding energy (ILBE) (Moore and Lockner, 2007; Morrow et al., 2000; Kosoglu et al., 2010; Sakuma and Suehara, 2015; Sanchez-Roa et al., 2017), whereby polar water molecules are bonded to layer surfaces in proportion to surface energy and increasing hydrophilicity. Whilst the structural charge in kaolinite crystals is low, in montmorillonite the charge is large due to the low crystallinity of the mineral and isomorphic substitutions on the silica tetrahedra (García-Romero and Suarez, 2018; Karnland et al., 2016; Vidal and Dubacq, 2009). This charge is balanced by the interlayer cation, which as discussed above also has a control on the water content. High friction coefficients in phyllosilicates with high ILBE may in fact be an effect of how removal of interlayer water alters the d-spacing, and therefore ILBE, of the crystals.

The measured wet friction coefficients for Mg-montmorillonite and kaolinite in this work compare favourably to those summarised and measured by Morrow et al. (2017) and Behnsen & Faulkner (2012) respectively. All clays exhibit low permeability, especially in the presence of water (Behnsen and Faulkner, 2011). Faulkner et al. (2018) showed how these low permeability materials may additionally be affected by initial compaction or dilation in fully saturated tests, even when displacement rates are relatively slow. This issue is exacerbated the lower permeability the clay is. For water saturated tests, Morrow et al. (2017) have shown that differences in reported friction coefficients in montmorillonite (μ = 0.06-0.48) (in experiments carried out by Summers and Byerlee, 1977; Shimamoto and Logan, 1981; Logan and Rauenzahn, 1987; Morrow et al., 1992, 2000; Brown et al., 2003; Saffer and Marone, 2003; Ikari et al., 2007; Moore and Lockner, 2007; Behnsen and Faulkner, 2012, 2013) can largely be explained by the partial saturation of samples wherever insufficient time is allowed for pore-fluid pressures to equilibrate. Another second order variation for wet friction coefficients in the 2:1 swelling smectite can be produced by the cation type, which Behnsen and Faulkner (2013) have demonstrated can produce a two-fold difference in μ. Friction coefficient of Mg-montmorillonite in this study is almost identical to that of Behnsen and Faulkner (2013) (~0.11), however variations in the interlayer cation were shown to increase μ by up to ~0.15. In kaolinite, water saturated friction coefficients have been reported as ~0.2 to ~0.53 (Behnsen & Faulkner 2012), comparable to ~0.27 reported here. In this study, increase in steady state μ in the 1:1 sheet silicate with each measured decrease in absolute water content is gradual but shows a total increase of 0.22 (~0.27 to ~0.49; Figure 6). This is considered to represent the effect of removing free water from the external surfaces of 1:1 phyllosilicate crystals (Figure 2). A similar trend of increasing friction coefficient with decreasing humidity has been observed in alumina gouge (Frye & Marone, 2002) albeit with a smaller increase in μ of ~0.04 due to its lower capacity for water retention. In the 2:1 swelling smectite, a more marked increase in μ between Mg-montmorillonite samples not heated and those heated during preparation (from 0.22 to 0.57) may be explained by the additional mass of interlayer water being removed from montmorillonite during the heating stage (Figure 2,4,6).

For dry tests, as mentioned previously, the degree to which the samples are dry is often not constrained or quantified. Published laboratory μ values for 'dry' kaolinite gouge have been shown to vary between ~0.4 and ~0.85 (Behnsen and Faulkner, 2012). These μ values are consistent with thermally dried samples in this study (~0.42 to ~0.49), however it is unlikely that the level of 'dryness' can fully explain the spread of 'dry' values reported elsewhere, suggesting other factors are contributing. One such factor may be at what stage during an experiment μ is reported. Moore & Lockner (2004), for example, have reported μ after a greater amount of shear, often displaying some strain hardening, which is seen particularly in the sawcut slider geometry. Another contributing factor potentially accounting for slightly lower friction coefficients in this study (and smaller absolute differences between wet and dry experiments) is the influence of 14 % illite/muscovite in the kaolinite-rich gouge - minerals with a lower electrostatic component of surface energy and separation energy. Published 'dry' μ values for montmorillonite gouge are extremely variable (0.22-0.78) (Summers and Byerlee, 1977; Shimamoto and Logan, 1981; Logan and Rauenzahn, 1987; Morrow et al., 1992, 2000; Brown et al., 2003; Saffer and Marone, 2003; Ikari et al., 2007; Moore and Lockner, 2007; Behnsen and Faulkner, 2012, 2013), yet again the range is comparable to those detailed in this study (0.19-0.57). Whilst the large range in published values could potentially also be partially explained by cation type, elevated pore pressure and variable water contents (Kosoglu et al., 2010; Behnsen and Faulkner, 2013; Morrow et al., 2017), this study shows clearly the marked effect of dehydration on the friction coefficient. This data is in agreement with Ikari et al. (2007), where μ values for Ca-montmorillonite under 100 MPa normal stress increase from ~0.03 to ~0.41 as water contents decrease from ~19 wt% to ~2 wt%.

Other notable observations can be made from these experiments on how water affects the evolution of phyllosilicate strength which is not necessarily due to the *level* of 'dryness'. More saturated clay gouges attain an observable peak yield stress before weakening to a lower steady state, whereas drier clay gouges undergo a more gradual increase in stress towards steady state (Figure 5). Similar trends have also been observed in alumina (Frye and Marone, 2002), and may be attributed to the development of Riedel- (R) and P-shears during early compaction, which may localise into Boundary- (Y) shears at peak stress (Logan et al., 1992; Haines et al., 2013) (Figure 8). As previously mentioned, stress peaks may also arise in low permeability samples during initial loading as water is expelled from pore space and crystal surfaces of clays; this occurs wherever pore-fluid pressures have not had sufficient time to equilibrate (Haines et al., 2013; Morrow et al., 2017; Faulkner et al., 2018). Where water films have been fully removed by heating, extra consolidation may be required to compact the clay grains, but μ is not reduced.

4.2 Evolution of Rate & State Parameters

The parameters within the rate and state formulation are not physical parameters, although many authors have attempted to relate them to physical processes in order to allow extrapolation beyond the conditions at which they were measured. By conducting experiments at various saturation states and noting how a, b and d_c respond, some insight can be gained into the deformation processes.

a-b values, which represent the frictional stability of a material (Figure 1), are typically positive (velocity-strengthening) in clays. In general, at an effective pressure of 60 MPa, a-b values for clays interpreted to have higher water contents are greater than those of drier clays (Figure 7a), suggesting that some type of fluid-assisted strengthening is taking place, perhaps related to the dissolution, transport and precipitation of other soluble phases within the gouge (e.g. Pluymakers and Spiers, 2015), however the relevant chemical conditions and timescales allowing these processes have not been considered in detail. Reducing the absolute water content of kaolinite gouge appears to change the effectiveness of the dominant deformation mechanisms, resulting in greater rate and state effects in samples that have been dried. The specific drying method applied to kaolinite gouge, however, does not seem to significantly affect results. In Mg-montmorillonite, samples that have been thermally dried appear to have markedly greater rate and state effects than those that have been dried at room humidity: our data show that in its driest state, a-b values for Mg-montmorillonite decrease to ~0.0025-0.0045 from ~0.0055-0.008 under room humidity conditions. Whilst Morrow et al. (2017) showed that comparable a-b values for Mg-montmorillonite increase in drier states, with respect to saturated conditions, to 0.006-0.01, Ikari et al. (2007) showed that a-b values decrease to <~0.01 and may even become negative when water contents are reduced to <4.5 wt%. Saturated a-b values for Mg-montmorillonite reported here (~0.0034-0.0045) are generally higher than those reported by Logan et al. (1992) (0.0005), Ikari et al. (2007) (~0-0.0025), Tembe et al. (2010) (0.0005) and Morrow et al. (2017) (0.0002-0.0069) at comparable stresses and sliding velocities.

With regards to the specific parameters, the rate variable, a, is a material-dependent velocity scaling factor (Figure 1), suggested to be a thermally-controlled Arrhenius mechanism (Dieterich and Kilgore, 1994; Rice et al., 2001; Bhattacharya et al., 2017; Aharonov and Scholz, 2018). a values for saturated Mg-montmorillonite in this study (~0.0028 to ~0.0038) (Figure 7b) are comparable to the lowest values presented by Logan & Rauenzahn (1987) (0.001 to 0.095). Whilst the rate parameter is lower in saturated Mg-montmorillonite samples, no clear trend is evident to speculate on the influence of *degree* of saturation, other than the fact that the rate effect is larger in drier Mg-montmorillonite. a values for kaolinite initially display a decreasing trend with as water content is reduced, reaching a minimum in vacuum dried, room humidity samples (Figure 7b), however values within the same range are exhibited in the driest samples, suggesting that this trend may be insignificant. The b value is the scaling factor for the state response to a step in sliding velocity (Figure 1), interpreted to relate to the strength of asperities in contact (i.e. quality of the contact surface) (Rice et al., 2001; Li et al., 2011) or healing of the contact surface area (Dieterich and Kilgore, 1996). Strength recovery during frictional sliding has been shown to be limited for phyllosilicate-rich materials (Carpenter et al., 2016), and healing is particularly negligible where humidity is low (Dieterich and Conrad, 1984; Frye and Marone, 2002). In this study, the b value appears to be dependent on degree of saturation in both clay types (Figure 7c). The state effect is magnified as samples become drier, apparently with a marked increase once heat is applied during the drying stage. This trend broadly corresponds to that seen in similar humidity-dependent experiments on alumina (Frye & Marone, 2002). Slight negative b values (Figure 7c) imply an increase in contact area with velocity in samples with a higher water content.

The characteristic distance, d_c, required for μ to exponentially decay to a new steady state, b (Figure 1) is thought relate to surface roughness and particle size; more specifically the slip necessary to renew surface contacts (Marone, 1998). Time-dependent healing (strength recovery, expressed as the parameter b) and velocity-dependent sliding are considered to be material constants acting in parallel (Dieterich, 1981; Dieterich and Conrad, 1984; Beeler et al., 1994; Beeler and Tullis, 1995; Marone, 1998). Observations here (Figure 7c,d) support the conclusion that fluid-assisted, time-dependent healing mechanisms are operative in gouge containing water but are effectively switched off in the driest phyllosilicates. Both b and d_c values are strongly controlled by the presence of water in both kaolinite and Mg-montmorillonite samples, and removal of water dramatically reduces d_c by up to one order of magnitude in kaolinite, and up to two orders of magnitude in thermally dried Mg-montmorillonite (Figure 7d). It seems clear that whatever deformation mechanisms are operating during frictional sliding are strongly influenced by the presence of water. Candidate deformation mechanisms that have been suggested in the literature include sub-critical crack growth, dissolution-precipitation creep (pressure solution), dislocation creep (hydrolytic weakening), or hydrogen bonding between adsorbed water molecules (c.f. Bos et al., 2000; Bos & Spiers, 2001; Chester, 1995; den Hartog et al., in press; Dieterich & Kilgore, 1994; Hickman & Evans, 1995; Kronenberg & Tullis, 1984; Rutter, 1983; Rutter & Mainprice, 1978), all of which would have an Arrhenius component. Further experiments conducted at a range of temperatures might help to further characterise the response of rate and state parameters to changing physical conditions and identify the principal deformation mechanisms.

4.3 Evolution of strength, stability, and microstructure

This study suggests that the level of ‘dryness’ also has a direct influence on the microstructure formed during shear, even when all other factors are kept constant. A decrease in frictional stability in drier clay gouges may be an inherent material property related to the evolution of microstructures and changes in the quality of surface contact, asperity contact area and angle.

Shear strain in gouge tends to concentrate along well-developed weak zones that control the overall strength of the material (Collettini et al., 2009; Lockner et al., 2011), which is most evident here in saturated gouges (Figure 8). The width of localised shear zones (between Y boundary shears) appears to decrease as water is removed from the sample (e.g. from ~500 µm in saturated kaolinite to <200 µm in vacuum dry + heated kaolinite) (Figure 8a-c and j-l), however these observations must be treated with caution due to the fragility and potential distortion of microstructure during drying and SEM preparation. More abundant P, R_1 and R' fractures in drier samples (Figure 8d-l) together with more distributed deformation requires less displacement on individual microfractures; deformation mechanisms acting on a smaller scale in drier samples may explain lower d_c values. Although more tests would be required to increase statistical significance, d_c values in the final velocity step (VS3) are generally lower than those from VS1 and VS2 (Figure 7d), which may be interpreted as the smoothing of principal boundary shears with increased time and displacement. Similar interpretations may be made regarding lower VS3 a and b values than in earlier velocity steps for the driest kaolinite samples (Figure 7b,c), suggesting that more displacement may be required to reduce frictional resistance and promote healing. Brittle structures may be locked in place until R_1 Riedel shears become interlinked with P shears, or a Y shear plane develops to reduce frictional strength (Figure 8). As the sample is sheared, healing may occur due to the reactivation of Riedel shears, enhancing fluid-assisted healing processes, or existing Riedel shears may heal and new shears form. Moore & Lockner (2007b) showed that saturated montmorillonite deforms along concentrated planes, whereas dry montmorillonite gouge (heated to 130˚C and prepared at room humidity) is subject to abrasion, wear and fracture during shear. Without microstructural analysis of Mg-montmorillonite samples and with little supporting evidence in the way of rate and state parameter data we are unable to draw similar conclusions for montmorillonite here.

It must be noted that some or all microstructures may be significantly influenced by drying methodology either before or after shear deformation. During air- or oven-drying, shrinkage may occur whereby remnant water between grains produces an inter-particle adhesion force, which may distort grain geometry (Aiyama et al., 2019). It may thus be inferred that our drying methodologies could have generated a weak grain fabric in the sample that could later be exploited during deformation. Additionally, post-experimental air-drying of gouge wafers may have further distorted microstructures generated during shear deformation. Drying and deformation microstructures have not been differentiated in this study, however upon the recommendation of Aiyama et al. (2019), freeze-drying of gouge samples will be considered for future studies involving more detailed microstructural analyses.

4.4 Implications of Study for Fault Slip in Nature and Experiments

Understanding the individual factors controlling frictional strength and stability in clay fault gouges, and the dehydration properties of individual phyllosilicates within them, is crucial to understanding fault mechanics, in particular the operative grain-scale deformation mechanisms. Crustal strength may be significantly overestimated by strength envelopes if the effects of fluid-assisted deformation mechanisms in fault zones are not accounted for (Bos and Spiers, 2000). Maximum (i.e. truly dry) friction coefficient in phyllosilicates is only achieved under careful laboratory conditions and saturated data is most likely to be observed in nature. That being said, increased dehydration, mechanical consolidation and mineral transformation may occur with depth (Marone and Scholz, 1988; Saffer and Marone, 2003; Ikari et al., 2009b), meaning that partially saturated to ‘dry’ data may be more applicable to regions of high geothermal gradients and poor fracture connectivity. Partially saturated data may also be applicable to caprocks forming part of a carbon capture and storage project, where drying clays potentially leading to increased permeability and fault strength is of some concern (Armitage et al., 2010; De Jong et al., 2014; Vilarrasa and Carrera, 2015). With increasing depth, both water content and the interlayer space decrease in 2:1 swelling smectites (Figure 2). Although it is possible for two or more mineral hydration states to coexist (Schleicher et al., 2013), many fault zones have been described where release of mineral-bound water from phyllosilicates appears to occur in stages at particular metamorphic pressure-temperature conditions, such as the sepiolite-bearing Galera Fault Zone (Sanchez-Roa et al., 2018) and the saponite-bearing San Andreas Fault, as observed via the SAFOD core (Carpenter et al., 2012; Holdsworth et al., 2011; Lockner et al., 2011). At average geothermal gradients, montmorillonite with two interstitial water layers can occur naturally at ~4-6km and dehydrates fully between ~6 and ~11km (Bird et al., 1984). Rates of dehydration with depth have been shown, in this study and elsewhere, to vary not only with pressure and temperature but also with phyllosilicate crystal structure and the interlayer cation type (Sanchez-Roa et al., 2018; Vidal and Dubacq; 2009).

The methodology used when preparing samples for ‘dry’ friction tests in the laboratory should be carefully considered. Firstly, friction coefficients of rock that has been ground and mixed during sample preparation may be greater than that of a natural fault where fabric has developed and weak materials have localised, thus gouge may be even weaker in its undisturbed state than in laboratory measurements (Collettini et al., 2009; Lockner et al., 2011). The combination of elevated pore pressures and development of strongly foliated layers with low frictional strength has been used to explain exceptionally weak faults (Faulkner and Rutter, 2001; Lockner et al., 2011; Behnsen and Faulkner, 2012). Secondly, heating samples to remove water films from clay grain surfaces is essential, especially in 2:1 sheet silicates. Failure to do this results in huge variability in friction coefficients and markedly different constitutive parameters. Performing experiments under vacuum appears to aid water removal in some clays (e.g. kaolinite) but has a minor effect overall relative to the effect of heating. In order to maintain good data compatibility in clay friction experiments between laboratories, fully equilibrated saturated samples should also be used. The low permeability of clays, particularly montmorillonite, slows the attainment of fluid pressure equilibrium (Morrow et al., 2017) leading to erroneous predictions of μ (Morrow et al., 2017; Faulkner et al., 2018). Care must be taken when considering published data on frictional parameters for sheet silicates. This study has followed the guidelines of Faulkner et al. (2018) and Morrow et al. (2017) in finding a balance between test geometry, strain rate, compaction rate, and fluid expulsion that leads to an acceptably equilibrated fluid pressure. If data are to be presented for unsaturated clays, the drying methodology should be outlined in full, and samples should be heated thoroughly under vacuum immediately prior to testing.

5. Conclusions

These initial tests provide constraints on the impact of clays on fault behaviour as well as the optimal experimental techniques used to study them, most notably:

- Saturation state has a large effect on strength and stability of clay-filled faults, which is much more pronounced in 2:1 swelling smectites than 1:1 sheet silicates. Friction coefficient increases by up to a factor of 3 in Mg-montmorillonite and by a factor of 2 in a kaolinite-rich gouge with increased 'dryness'.
- Published μ values are generally consistent with those presented in this study, however it is unlikely that the level of 'dryness' can fully explain the spread of values, particularly those for dry friction coefficients. This suggests that other factors are contributing, such as crystal structure, layer charge and cation type, grain properties, and at what stage in the experiment is reported.
- Rate and state parameters evolve with saturation state, such that as water is removed clay gouges become less stable (a-b values decrease), and the amount of displacement or time required to establish a new steady state friction coefficient upon a change in sliding velocity (d_c) decreases.

- Fluid-assisted deformation mechanisms operating during frictional sliding are strongly influenced by the presence of water, which also has a direct influence on the microstructure formed during shear, even when all other factors are kept constant.
- So long as the sample has been heated, the level of vacuum appears to have little effect on friction coefficient, although it may promote a lower yield. If data are to be presented for unsaturated clays, the drying methodology should be outlined in full, and samples should be heated thoroughly under vacuum prior to testing as soon as possible thereafter.

Acknowledgements

Funding: This work was supported by the Natural Environment Research Council (NERC) as part of an EAO Doctoral Training Partnership and a standard grant [grant numbers NE/L002469/1, NE/P002943/1], whose support is gratefully acknowledged.

Our thanks are also extended to the two reviewers for their constructive feedback that helped to improve the article; Steve Crowley for his assistance in the design of the vacuum setup; Gary Coughlan for technical assistance in University of Liverpool's Rock Deformation Laboratory; Yan Lavallée, Sabine den Hartog and Marieke Rempe for their invaluable discussions; and to University of Liverpool's SEM and Thermal Laboratories.

References

Aharonov, E., Scholz, C.H., 2018. A Physics-Based Rock Friction Constitutive Law: Steady State Friction. Journal of Geophysical Research: Solid Earth 123, 1591–1614.

Aiyama, K., Mizoguchi, K., Hirano, K., Takizawa, S., 2019. Effects of sample preparation on the microstructural signatures of faulting in clay-bearing fault gouge. Journal of Structural Geology 126, 100-108.

Aksu, I., Bazilevskaya, E., Karpyn, Z.T., 2015. Swelling of clay minerals in unconsolidated porous media and its impact on permeability. GeoResJ 7, 1–13.

Armitage, P.J., Worden, R.H., Faulkner, D.R., Aplin, A.C., Butcher, A.R., Iliffe, J., 2010. Diagenetic and sedimentary controls on porosity in Lower Carboniferous fine-grained lithologies, Krechba field, Algeria: A petrological study of a caprock to a carbon capture site. Marine and Petroleum Geology 27, 1395–1410.

Bala, P., Samantaray, B.K., Srivastava, S., 2000. Dehydration transformation in Ca-montmorillonite. Bulletin of Materials Science 23, 61-67.

Beeler, N.M., Tullis, T.E., 1995. Implications of Coulomb plasticity for the velocity dependence of experimental faults. Pure and Applied Geophysics 144, 251–276.

Beeler, N.M., Tullis, T.E., Weeks, J.D., 1994. The roles of time and displacement in the evolution effect in rock friction. Geophysical Research Letters 21, 1987–1990.

Behnsen, J., Faulkner, D.R., 2013. Permeability and frictional strength of cation-exchanged montmorillonite. Journal of Geophysical Research: Solid Earth 118, 2788–2798.

Behnsen, J., Faulkner, D.R., 2012. The effect of mineralogy and effective normal stress on frictional strength of sheet silicates. Journal of Structural Geology 42, 49–61.

Bethke C. M., 1986. Inverse hydrologic analysis of the distribution and origin of Gulf Coast-type geopressured zones. Journal of Geophysical Research 91, 6535–6545.

Bhattacharya, P., Rubin, A.M., Beeler, N.M., 2017. Does fault strengthening in laboratory rock friction experiments really depend primarily upon time and not slip? Journal of Geophysical Research: Solid Earth 122, 6389–6430.

Biegel, R.L., Sammis, C.G., Dieterich, J.H., 1989. The frictional properties of a simulated gouge having a fractal particle distribution. Journal of Structural Geology 11, 827–846.

Blanpied, M., Tullis, T.E., Weeks, D., 1998. Effects of slip, slip rate, and shear heating on the friction of granite. Journal of Geophysical Research 103, 489–511.

Bos, B., Peach, C.J., Spiers, C.J., 2000. Frictional-viscous flow of simulated fault gouge caused by the combined effects of phyllosilicates and pressure solution. Tectonophysics 327, 173–194.

Bos, B., Spiers, C.J., 2001. Experimental investigation into the microstructural and mechanical evolution of phyllosilicate-bearing fault rock under conditions favouring pressure solution. Journal of Structural Geology 23, 1187–1202.

Bos, B., Spiers, C.J., 2000. Effect of phyllosilicates on fluid-assisted healing of gouge-bearing faults. Earth and Planetary Science Letters 184, 199–210.

Brown, K.M., Kopf, A., Underwood, M.B., Weinberger, J.L., 2003. Compositional and fluid pressure controls on the state of stress on the Nankai subduction thrust: A weak plate boundary. Earth and Planetary Science Letters 214, 589–603.

Byerlee, J.D., 1978. Friction of rocks. Pure and Applied Geophysics PAGEOPH 116, 615–626.

Carpenter, B.M., Saffer, D.M., Marone, C., 2012. Frictional properties and sliding stability of the San Andreas fault from deep drill core. Geology 40(8), 759-762.

Carpenter, B.M., Ikari, M.J., Marone, C., 2016. Laboratory observations of time-dependent frictional strengthening and stress relaxation in natural and synthetic fault gouges. Journal of Geophysical Research: Solid Earth 121, 1183–1201.

Chester, F.M., 1995. A rheologic model for wet crust applied to strike-slip faults. Journal of Geophysical Research 100, 33–44.

Collettini, C., Niemeijer, A.R., Viti, C., Marone, C., 2009. Fault zone fabric and fault weakness. Nature 462, 907–910.

Colten-Bradley, V.A., 1987. Role of Pressure in Smectite Dehydration - Effects on Geopressure and Smectite-to-Illite Transformation. The American Association of Petroleum Geologists Bulletin 71(11), 1414-1427.

Crawford, B.R., Faulkner, D.R., Rutter, E.H., 2008. Strength, porosity, and permeability development during hydrostatic and shear loading of synthetic quartz-clay fault gouge. Journal of Geophysical Research: Solid Earth 113, 1–14.

De Jong, S.M., Spiers, C.J., Busch, A., 2014. Development of swelling strain in smectite clays through exposure to carbon dioxide. International Journal of Greenhouse Gas Control 24, 149–161.

Den Hartog, S.A.M., 2013. Frictional behaviour of megathrust fault gouges under in-situ subduction zone conditions. PhD Thesis, University of Liverpool.

Den Hartog, S.A.M., Faulkner, D.R., Spiers, C.J., In Press. Low friction coefficient of phyllosilicate fault gouges quantitatively explained. Journal of Geophysical Research.

Diamond, S., Kinter, E.B., 1958. Surface areas of clay minerals as derived from measurements of glycerol retention. Clays and Clay Minerals 5, 334–347.

Dieterich, J.H., 1981. Constitutive Properties of Faults With Simulated Gouge. In: Carter, N., Friedman, M., Logan, J.M., Stearns, D.W. (Eds.), Mechanical Behavior of Crustal Rocks: The Handin Volume. American Geophysical Union, 103–120.

Dieterich, J.H., 1979. Modeling of rock friction: 1. Experimental results and constituve equations. Journal of Geophysical Research 84, 2161–2168.

Dieterich, J.H., 1978. Time-dependent friction and the mechanics of stick-slip. Pure and Applied Geophysics 116, 790–806.

Dieterich, J.H., 1972. Time-dependent friction in rocks. Journal of Geophysical Research 77, 3690–3697.

Dieterich, J.H., Conrad, G., 1984. Effect of Humidity on Time- and Velocity-Dependent Friction in Rocks. Journal of Geophysical Research 89, 4196–4202.

Dieterich, J.H., Kilgore, B.D., 1996. Imaging surface contacts: power law contact distributions and contact stresses in quartz, calcite, glass and acrylic plastic. Tectonophysics 256, 219–239.

Dieterich, J.H., Kilgore, B.D., 1994. Direct Observation of Frictional Contacts: New Insights for State-dependent Properties. Pure and Applied Geophysics 143, 283–301.

Faulkner, D.R., Armitage, P.J., 2013. The effect of tectonic environment on permeability development around faults and in the brittle crust. Earth and Planetary Science Letters 375, 71–77.

Faulkner, D.R., Mitchell, T.M., Behnsen, J., Hirose, T., Shimamoto, T., 2011. Stuck in the mud? Earthquake nucleation and propagation through accretionary forearcs. Geophysical Research Letters 38, 1–5.

Faulkner, D.R., Mitchell, T.M., Rutter, E.H., Cembrano, J., 2008. On the structure and mechanical properties of large strike-slip faults. Geological Society, London, Special Publications 299, 139–150.

Faulkner, D.R., Rutter, E.H., 2001. Can the maintenance of overpressured fluids in large strike-slip fault zones explain their apparent weakness? Geology 29, 503–506.

Faulkner, D.R., Rutter, E.H., 2000. Comparisons of water and argon permeability in natural clay-bearing fault gouge under high pressure at 20°C. Journal of Geophysical Research 105, 16415-16426.

Faulkner, D.R., Sanchez-Roa, C., Boulton, C., den Hartog, S.A.M., 2018. Pore-fluid Pressure Development in Compacting Fault Gouge in Theory, Experiments, and Nature. Journal of Geophysical Research: Solid Earth 1–16.

Frye, K.M., Marone, C., 2002. Effect of humidity on granular friction at room temperature. Journal of Geophysical Research: Solid Earth 107, 2309.

García-Romero, E., Suarez, M., 2018. A structure-based argument for non-classical crystal growth in natural clay minerals. Mineralogical Magazine 82, 171-180.

Giese, R.F., 1979. Hydroxyl Orientations in 2:1 Phyllosilicates. Clays and Clay Minerals 27, 213–223.

Giese, R.F., 1978. Electrostatic Interlayer Forces of Layer Structure Minerals. Clays and Clay Minerals 26, 51–57.

Haines, S.H., Kaproth, B., Marone, C., Saffer, D., Van der Pluijm, B., 2013. Shear zones in clay-rich fault gouge: A laboratory study of fabric development and evolution. Journal of Structural Geology 51, 206–225.

Hickman, S.H., Evans, B., 1995. Kinetics of pressure solution at halite-silica interfaces and intergranular clay films. Journal of Geophysical Research 100, 13113–13132.

Holdsworth, R.E., van Diggelen, E.W.E., Spiers, C.J., de Bresser, J.H.P., Walker, R.J., Bowen, L., 2011. Fault rocks from the SAFOD core samples: Implications for weakening at shallow depths along the San Andreas Fault, California. Journal of Structural Geology 33, 132-144.

Ikari, M.J., Marone, C., Saffer, D.M., 2011. On the relation between fault strength and frictional stability. Geology 39, 83–86.

Ikari, M.J., Saffer, D.M., Marone, C., 2007. Effect of hydration state on the frictional properties of montmorillonite-based fault gouge. Journal of Geophysical Research: Solid Earth 112, 1–12.

Ikari, M.J., Saffer, D.M., Marone, C., 2009a. Frictional and hydrologic properties of clay-rich fault gouge. Journal of Geophysical Research 114, 1–18.

Ikari, M.J., Saffer, D.M., Marone, C., 2009b. Frictional and hydrologic properties of a major splay fault system, Nankai subduction zone. Geophysical Research Letters 36, 1–5.

Inoue, M., Utada, A., 1988. Smectite-to-chlorite transformation in thermally metamorphosed volcanoclastic rocks in the Kamikita area, northern Honshu, Japan. American Mineralogist 76, 628-640.

Israelachvili, J.N., McGuiggan, P.M., Homola, A.M., 1988. Dynamic Properties of Molecularly Thin Liquid Films. Science 240, 189–191.

Karnland, O., Olsson, S., Nilssen, U., 2016. Mineralogy and sealing properties of various bentonites and smectite-rich clay materials. Svensk Kärnbränslehantering AB Technical Report TR-06-30, Stockholm, 113p.

Kell, G.S., 1975. Density, Thermal Expansivity, and Compressibility of Liquid Water from 0" to 150°C: Correlations and Tables for Atmospheric Pressure and Saturation Reviewed and Expressed on 1968 Temperature Scale. Journal of Chemical and Engineering Data 2, 97–105.

Kosoglu, L.M., Bickmore, B.R., Filz, G.M., Madden, A.S., 2010. Atomic force microscopy method for measuring smectite coefficients of friction. Clays and Clay Minerals 58, 813–820.

Kronenberg, A.K., Tullis, J., 1984. Flow strengths of quartz aggregates: Grain size and pressure effects due to hydrolytic weakening. Journal of Geophysical Research: Solid Earth 89, 4281–4297.

Lázaro, B.B., 2015. Halloysite and Kaolinite: Two clay minerals with geological and technological importance. La Revista de la Real Academia de Ciencas Zaragoza 70, 1-33.

Likhachev, E.R., 2003. Dependence of water viscosity on temperature and pressure. Technical Physics 48, 514–515.

Linker, M.F., Dieterich, J.H., 1992. Effects of variable normal stress on rock friction: Observations and constitutive equations. Journal of Geophysical Research 97, 4923–4940.

Lockner, D.A., Morrow, C.A., Moore, D.E., Hickman, S.H., 2011. Low strength of deep San Andreas fault gouge from SAFOD core. Nature 472, 82–86.

Logan, J.M., Dengo, C.A., Higgs, N.G., Wang, Z.Z., 1992. Fabrics of Experimental Fault Zones: Their Development and Relationship to Mechanical Behavior. Fault Mechanics and Transport Properties of Rocks. 33–67.

Logan, J.M., Rauenzahn, K.A., 1987. Frictional dependence of gouge mixtures of quartz and montmorillonite on velocity, composition and fabric. Tectonophysics 144, 87–108.

Mackenzie, R.C., 1957. Hydration and hydroxylation with special reference to montmorillonite. Geologiska Föreningen i Stockholm Förhandlingar 79, 58–61.

Mair, K., Marone, C., 1999. Friction of simulated fault gouge for a wide range of velocities and normal stresses. Journal of Geophysical Research 104, 28899–28914.

Marone, C., 1998. Laboratory-Derived Friction Laws and Their Application To Seismic Faulting. Annual Review of Earth and Planetary Sciences 26, 643–696.

Marone, C., Kilgore, B., 1993. Scaling of the critical slip distance for seismic faulting with shear strain in fault zones. Nature 362, 618–621.

Marone, C., Scholz, C.H., 1988. The Depth of Seismic Faulting and the Upper Transition from Stable to Unstable Slip Regimes. Geophysical Research Letters 15, 621–624.

Moore, D.E., Lockner, D.A., 2011. Frictional strengths of talc-serpentine and talc-quartz mixtures. Journal of Geophysical Research: Solid Earth 116, 1–17.

Moore, D.E., Lockner, D.A., 2007. Friction of the Smectite Clay Montmorillonite: A Review and Interpretation of Data. The Seismogenic Zone of Subduction Thrust Faults. 317–345.

Moore, D.E., Lockner, D.A., 2004. Crystallographic controls on the frictional behavior of dry and water-saturated sheet structure minerals. Journal of Geophysical Research 109, 1–16.

Moore, D. M., Reynolds Jr., R.C., 1997. X-Ray Diffraction and the Identification and analysis of Clay Minerals, 2nd edition, New York, Oxford University Press, 378p.

Morrow, C.A., Moore, D.E., Lockner, D.A., 2017. Frictional strength of wet and dry montmorillonite. Journal of Geophysical Research: Solid Earth 122, 3392–3409.

Morrow, C.A., Moore, D.E., Lockner, D.A., 2000. The effect of mineral bond strength and adsorbed water on fault gouge frictional strength. Geophysical Research Letters 27, 815–818.

Morrow, C.A., Radney, B., Byerlee, J.D., 1992. Frictional Strength and the Effective Pressure Law of Montmorillonite and lllite Clays. International Geophysics 51, 69–88.

Noda, H., Shimamoto, T., 2009. Constitutive properties of clayey fault gouge from the Hanaore fault zone, southwest Japan. Journal of Geophysical Research: Solid Earth 114, 1–29.

Noda, H., Shimamoto, T., 2005. Thermal pressurization and slip-weakening distance of a fault: An example of the Hanaore fault, southwest Japan. Bulletin of the Seismological Society of America.

Pluymakers, A.M.H., Spiers, C.J., 2015. Compaction creep of simulated anhydrite fault gouge by pressure solution: Theory v. experiments and implications for fault sealing. In: Faulkner, D. R., Mariani, E., Mecklenburgh, J. (eds), 2015. Rock Deformation from Field, Experiments and Theory: A Volume in Honour of Ernie Rutter. Geological Society, London, Special Publications 409, 107–124.

Reinen, L.A., Weeks, J.D., Tullis, T.E., 1994. The frictional behavior of lizardite and antigorite serpentinites: Experiments, constitutive models, and implications for natural faults. Pure and Applied Geophysics 143, 317–358.

Renard, F., Ortoleva, P., 1997. Water films at grain-grain contacts: Debye-Hückel, osmotic model of stress, salinity, and mineralogy dependence. Geochimica et Cosmochimica Acta 61, 1963–1970.

Rice, J.R., Lapusta, N., Ranjith, K., 2001. Rate and State Dependent Friction and the Stability of Sliding Between Elastically Deformable Solids. Journal of the Mechanics and Physics of Solids 49(9), 1865-1868.

Ruina, A.L., 1983. Slip Instability and State Variable Laws. Journal of Geophysical Research 88, 359–370.

Rutter, E.H., 1983. Pressure solution in nature, theory and experiment. Journal of the Geological Society 140, 725–740.

Rutter, E.H., Maddock, R.H., 1987. On the mechanical properties of synthetic kaolinite / quartz fault gouge. Terra Nova 4, 489–500.

Rutter, E.H., Maddock, R.H., Hall, S.H., White, S.H., 1986. Comparative microstructures of natural and experimentally produced clay-bearing fault gouges. Pure and Applied Geophysics 124, 3–30.

Rutter, E.H., Mainprice, D.H., 1978. The effect of water on stress relaxation of faulted and unfaulted sandstone. Pure and Applied Geophysics 116, 634–654.

Saffer, D.M., Frye, K.M., Marone, C., Mair, K., 2001. Laboratory results indicating complex and potentially unstable frictional behavior of smectite clay. Geophysical Research Letters 28, 2297–2300.

Saffer, D.M., Marone, C., 2003. Comparison of smectite- and illite-rich gouge frictional properties: Application to the updip limit of the seismogenic zone along subduction megathrusts. Earth and Planetary Science Letters 215, 219–235.

Sakuma, H., Suehara, S., 2015. Interlayer bonding energy of layered minerals: Implication for the relationship with friction coefficient. Journal of Geophysical Research: Solid Earth 120, 2212–2219.

Sánchez-Roa, C., Jiménez-Millán, J., Abad, I., Faulkner, D.R., Nieto, F., García-Tortosa, F.J., 2016. Fibrous clay mineral authigenesis induced by fluid-rock interaction in the Galera Fault Zone (Betic Cordillera, SE Spain) and its influence on fault gouge frictional properties. Applied Clay Science, 134, 275-288.

Sanchez-Roa, C., Faulkner, D.R., Boulton, C., Jimenez-Milan, J., Nieto, F., 2017. How phyllosilicate mineral structure affects fault strength in Mg-rich fault systems. Geophysical Research Letters 44, 5457–5467.

Sanchez-Roa, C., Vidal, O., Jiménez-Millán, J., Nieto, F., Faulkner, D. R., 2018. Implications of sepiolite dehydration for earthquake nucleation in the Galera Fault Zone: A thermodynamic approach. Applied Geochemistry 89, 219-228.

Schleicher, A. M., van der Pluijm, B.A., Warr, L.N., 2012. Chlorite-smectite clay minerals and fault behavior: new evidence from the San Andreas Fault Observatory at Depth (SAFOD) core. Lithosphere 4, 209–220.

Schleicher, A.M., Hofmann, H., van der Pluijm, B.A., 2013. Constraining clay hydration state and its role in active fault systems. Geochemistry Geophysics Geosystems 14, 1039–1052.

Scholz, C.H., 1998. Earthquakes and friction laws. Nature 391, 37–42.

Shimamoto, T., Logan, J.M., 1981. Effects of simulated clay gouges on the sliding behavior of Tennessee sandstone. Tectonophysics 75, 243–255.

Summers, R., Byerlee, J.D., 1977. A note on the effect of fault gouge composition on the stability of frictional sliding. International Journal of Rock Mechanics, Mining Sciences and Geomechanics 14, 155–160.

Takahashi, M., Mizoguchi, K., Masuda, K., Potential of phyllosilicate dehydration and dehydroxylation reactions to trigger earthquakes. Journal of Geophysical Research 114, B02207.

Tembe, S., Lockner, D.A., Wong, T., 2009. Constraints on the stress state of the San Andreas Fault with analysis based on core and cuttings from San Andreas Fault Observatory at Depth (SAFOD) drilling phases 1 and 2. Journal of Geophysical Research 114, 1–21.

Tetsuka, H., Katayama, I., Sakuma, H., Tamura, K., 2018. Effects of humidity and interlayer cations on the frictional strength of montmorillonite. Earth, Planets and Space 70, 1–9.

Underwood, M.B., 2007. Clay mineral composition and diagenesis: Effects on the location and behavior of faults in the frontal portions of subduction zones. Scientific Drilling 61–63.

Vidal, O., Dubacq, B. 2009. Thermodynamic modelling of clay dehydration, stability and compositional evolution with temperature, pressure and H2O activity. Geochimica et Cosmochimica Acta, 73, 6544-6564.

Vidal, J., Patrier, P., Genter, A., Beaufort, D., Dezayes, C., Glaas, C., Lerouge, C., Sanjuan, B., 2018. Clay minerals related to the circulation of geothermal fluids in boreholes at Rittershoffen (Alsace, France). Journal of Volcanology and Geothermal Research 349, 192–204.

Vilarrasa, V., Carrera, J., 2015. Geologic carbon storage is unlikely to trigger large earthquakes and reactivate faults through which CO_2 could leak. Proceedings of the National Academy of Sciences 112, 5938–5943.

Figure Captions

Figure 1: Schematic frictional response to steps in sliding velocity for **a)** velocity-strengthening friction and **b)** velocity-weakening friction (after Den Hartog, 2013). Samples tested here show velocity-strengthening behaviour and would not result in seismicity.

Figure 2: Crystal structures of **a)** 1:1 Kaolinite and **b)** 2:1 Mg-Montmorillonite. The latter can absorb more water due to the presence of interlayer surfaces, where water molecules are bonded to the interlayer cation (Mg). **c)** Interlayer water films affect the frictional properties of sheet materials by forming a low μ shear interstitial surface bound to T-O-T layers (T = tetrahedral, O = octahedral), or as free water to external surfaces.

Figure 3: **a)** Sample assembly setup prior to being placed into the pressure vessel, with schematic illustration of the configuration used (total length of schematic view ~75 mm). The configuration is jacketed, and silicon oil is used as the confining medium. In non-saturated experiments, a vacuum is applied to the sample through pore pressure access points (after Faulkner et al., 2018). **b)** Schematic representation of a vacuum connection to the sample assembly. Gauges are indicated by diagonal arrows; valves are indicated by crosses.

Figure 4: **a)** Results of Thermogravimetric Analysis (TGA) performed on initially room humidity kaolinite and montmorillonite. Samples were heated to 130 °C at 2 °Cmin^{-1} and held for 6 hours, before being heated further to 200 ˚C to investigate mass loss beyond temperatures used in sample preparation. **b)** Results of mass loss during heating to 130 °C in a vacuum oven with respect to the mass of initially room humidity kaolinite and montmorillonite.

Figure 5: Friction coefficient evolution with displacement for **a)** kaolinite-rich china clay and **b)** Mg-montmorillonite at different saturation states. Initial displacement rate was 0.3 microns per second. Velocity steps at 2.5 mm, 4 mm and 4.75 mm displacement represent an increase in displacement rate to 3 microns/second for 0.75 mm, before resuming to 0.3 microns/second. Effective pressure in each scenario was 60 MPa.

Figure 6: Summary of yield (dotted lines) and steady state (solid lines) friction coefficients for kaolinite-rich china clay (blue triangles and orange circles respectively) and Mg-montmorillonite (brown diamonds and green squares respectively), for each saturation state scenario. Ranges of minimum and maximum recorded data are shown for kaolinite.

Figure 7: a) a-b values; **b)** a values, **c)** b values and **d)** dc values for i) kaolinite-rich china clay and ii) Mg-montmorillonite for each saturation state scenario. Velocity steps (VS) 1 to 3 (2.5 mm, 4 mm and 5.5 mm displacement respectively) are displayed as green circles, blue triangles and red stars respectively. Mean error (standard deviation) is displayed as a scaled bar. Note that dc values are plotted on a log scale for clarity.

Figure 8: SEM image of typical microstructures exhibited in kaolinite-rich gouge, sheared to 6.25 mm displacement at 60MPa effective pressure, when **a)**, **b)** & **c)** saturated, **d)**, **e)** & **f)** at room humidity, **g)**, **h)** & **i)** vacuum dry and **j)**, **k)** & **l)** heated in a pressure vessel to 130 °C and allowed to cool before shearing. Shear direction in all images is dextral. Scale bars in the bottom left of each image represent 100 µm. The majority of the sample (light grey) is

interpreted using EDS to be largely kaolinite with minor illite/muscovite. Non-platy white areas are interpreted to be K-feldspar. Quartz is also present in minor quantities.

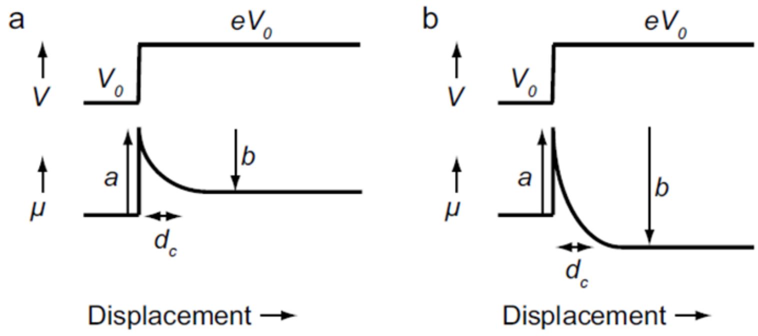

Figure 1

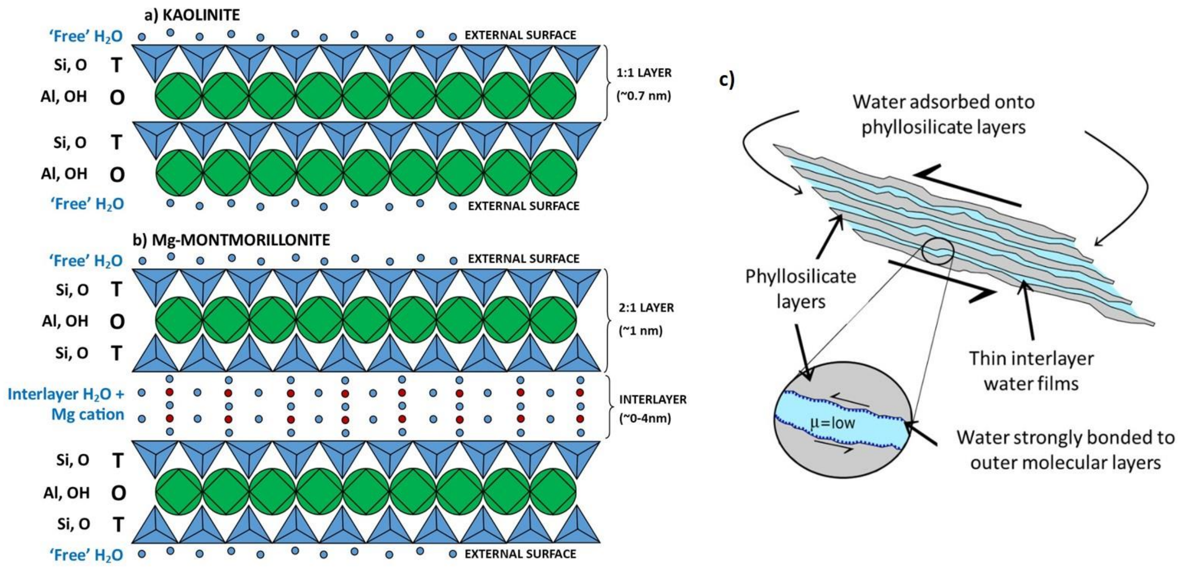
a) KAOLINITE
'Free' H_2O
EXTERNAL SURFACE
Si, O
T
Al, OH
O
1:1 LAYER
(~0.7 nm)
Si, O
T
Al, OH
O
'Free' H_2O
EXTERNAL SURFACE
b) Mg-MONTMORILLONITE
'Free' H_2O
EXTERNAL SURFACE
Si, O
T
Al, OH
O
Si, O
T
2:1 LAYER
(~1 nm)
Interlayer H_2O +
Mg cation
INTERLAYER
(~0-4nm)
Si, O
T
Al, OH
O
Si, O
T
'Free' H_2O
EXTERNAL SURFACE
c)
Water adsorbed onto
phyllosilicate layers
Phyllosilicate
layers
Thin interlayer
water films
μ=low
Water strongly bonded to
outer molecular layers

Figure 2

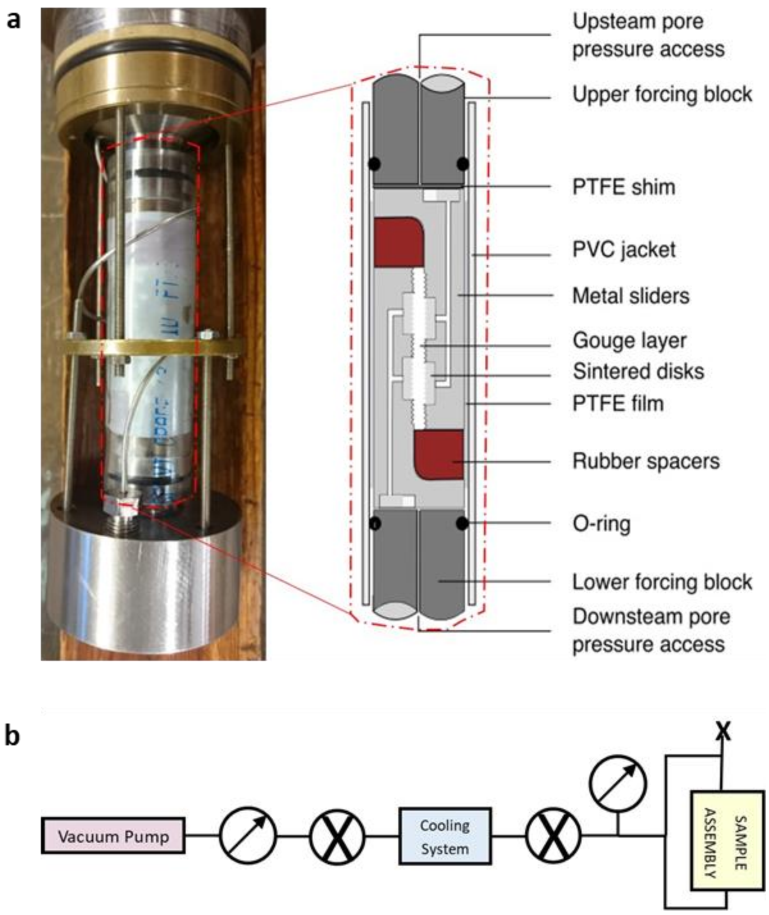
a
Upsteam pore pressure access
Upper forcing block
PTFE shim
PVC jacket
Metal sliders
Gouge layer
Sintered disks
PTFE film
Rubber spacers
O-ring
Lower forcing block
Downsteam pore pressure access
b
Vacuum Pump
Cooling System
SAMPLE ASSEMBLY
X

Figure 3

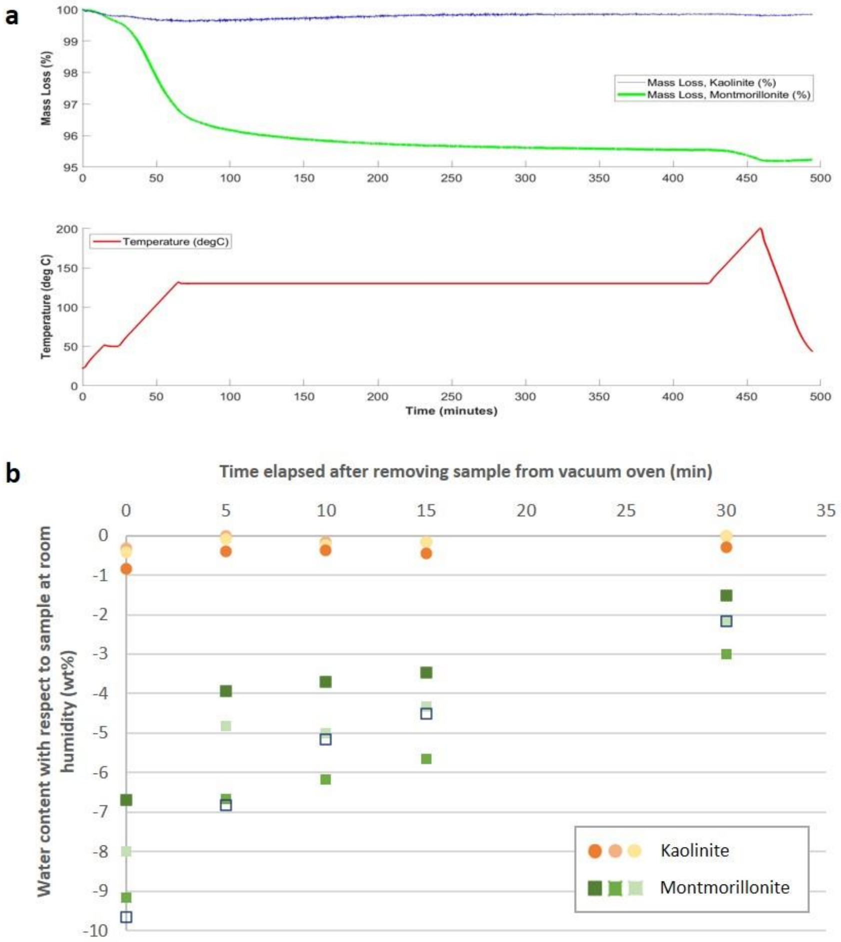
a
Mass Loss (%)
100
99
98
97
96
95
0
50
100
150
200
250
300
350
400
450
500
Mass Loss, Kaolinite (%)
Mass Loss, Montmorillonite (%)
Temperature (deg C)
200
150
100
50
0
Temperature (degC)
Time (minutes)
b
Time elapsed after removing sample from vacuum oven (min)
0
5
10
15
20
25
30
35
Water content with respect to sample at room humidity (wt%)
0
-1
-2
-3
-4
-5
-6
-7
-8
-9
-10
Kaolinite
Montmorillonite

Figure 4

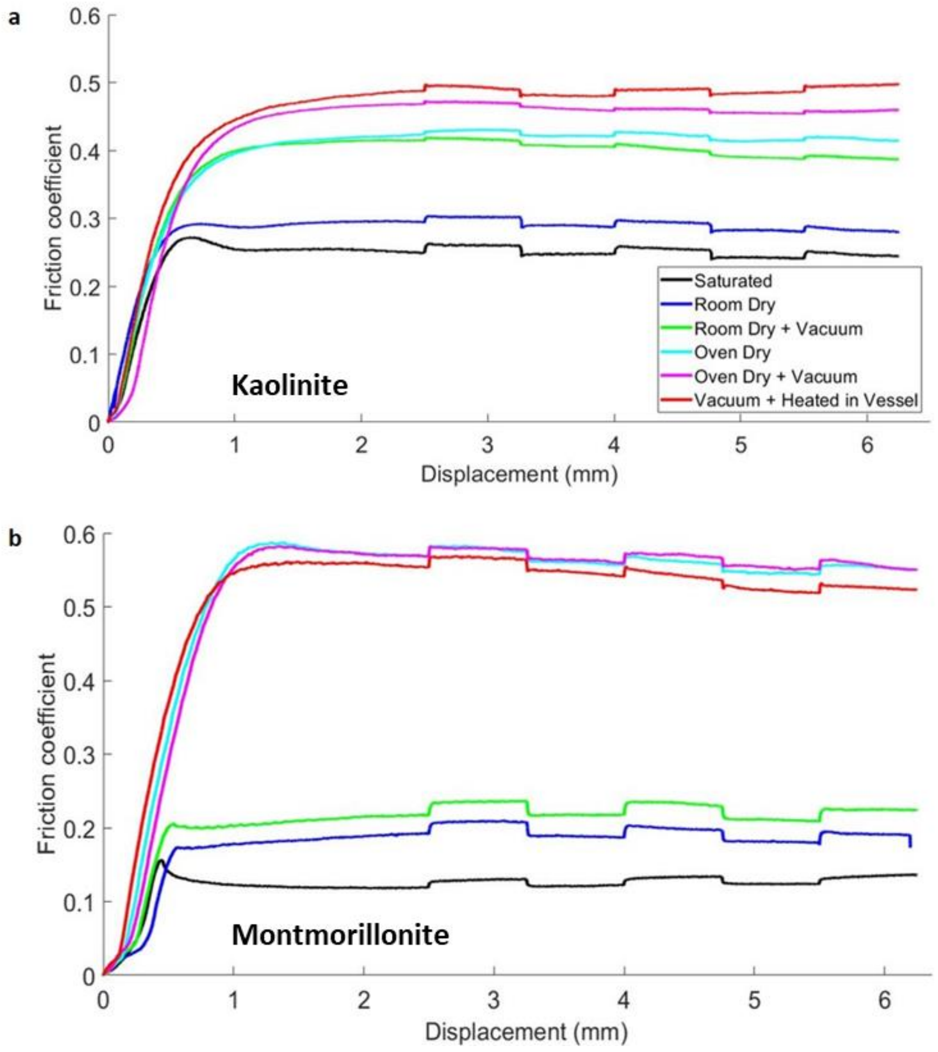
a
0.6
0.5
0.4
0.3
0.2
0.1
0
Friction coefficient
0
1
2
3
4
5
6
Displacement (mm)
Kaolinite
Saturated
Room Dry
Room Dry + Vacuum
Oven Dry
Oven Dry + Vacuum
Vacuum + Heated in Vessel
b
0.6
0.5
0.4
0.3
0.2
0.1
0
Friction coefficient
0
1
2
3
4
5
6
Displacement (mm)
Montmorillonite

Figure 5

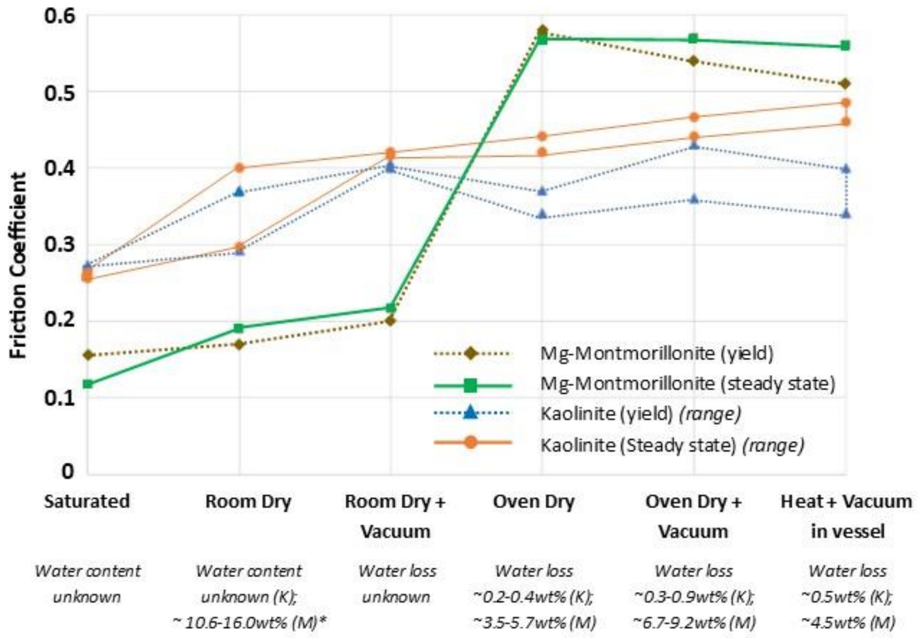
0.6
0.5
0.4
0.3
0.2
0.1
0
Friction Coefficient
Mg-Montmorillonite (yield)
Mg-Montmorillonite (steady state)
Kaolinite (yield) (range)
Kaolinite (Steady state) (range)
Saturated
Room Dry
Room Dry + Vacuum
Oven Dry
Oven Dry + Vacuum
Heat + Vacuum in vessel
Water content unknown
Water content unknown (K); ~ 10.6-16.0wt% (M)*
Water loss unknown
Water loss ~0.2-0.4wt% (K); ~3.5-5.7wt% (M)
Water loss ~0.3-0.9wt% (K); ~6.7-9.2wt% (M)
Water loss ~0.5wt% (K); ~4.5wt% (M)

Figure 6

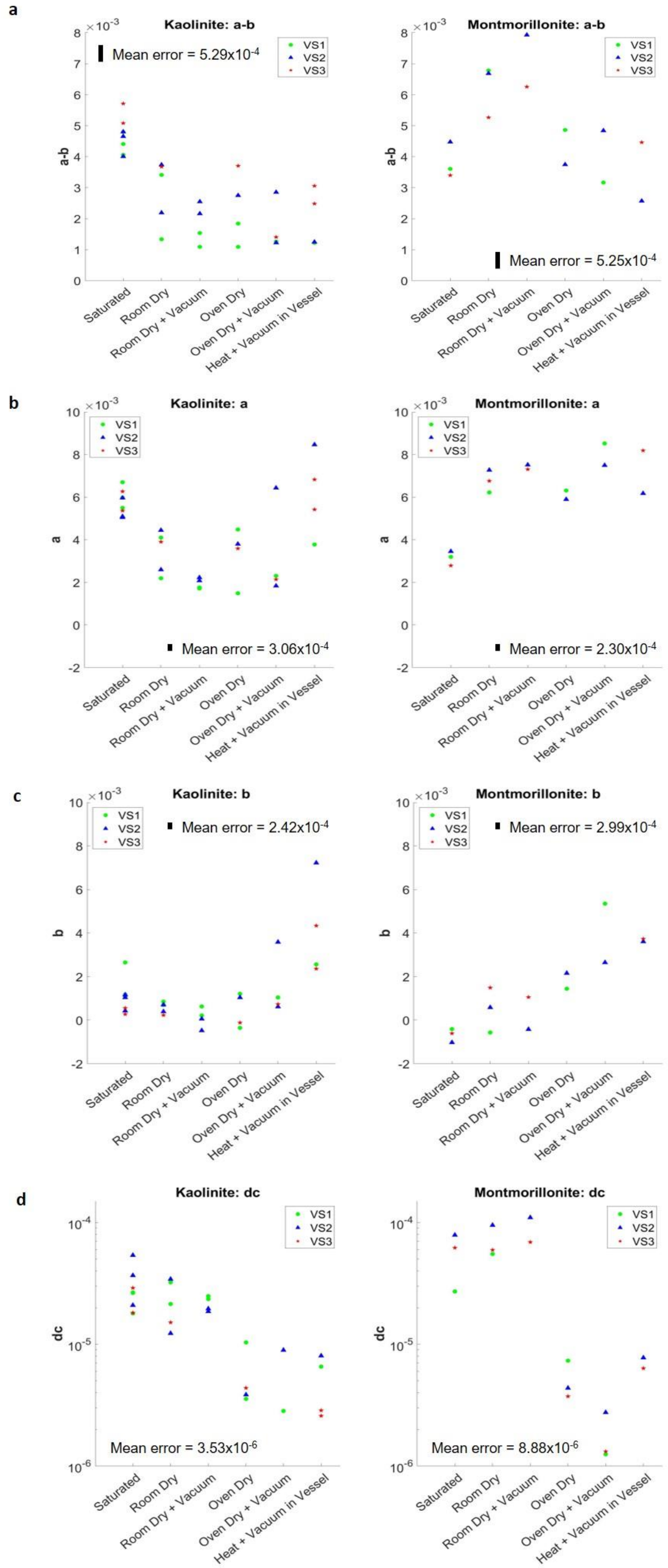
a
Kaolinite: a-b
Mean error = 5.29x10^-4
Montmorillonite: a-b
Mean error = 5.25x10^-4
a-b
×10^-3
b
Kaolinite: a
Mean error = 3.06x10^-4
Montmorillonite: a
Mean error = 2.30x10^-4
a
c
Kaolinite: b
Mean error = 2.42x10^-4
Montmorillonite: b
Mean error = 2.99x10^-4
b
d
Kaolinite: dc
Mean error = 3.53x10^-6
Montmorillonite: dc
Mean error = 8.88x10^-6
dc
10^-4
10^-5
10^-6
VS1
VS2
VS3
Saturated
Room Dry
Room Dry + Vacuum
Oven Dry
Oven Dry + Vacuum
Heat + Vacuum in Vessel

Figure 7

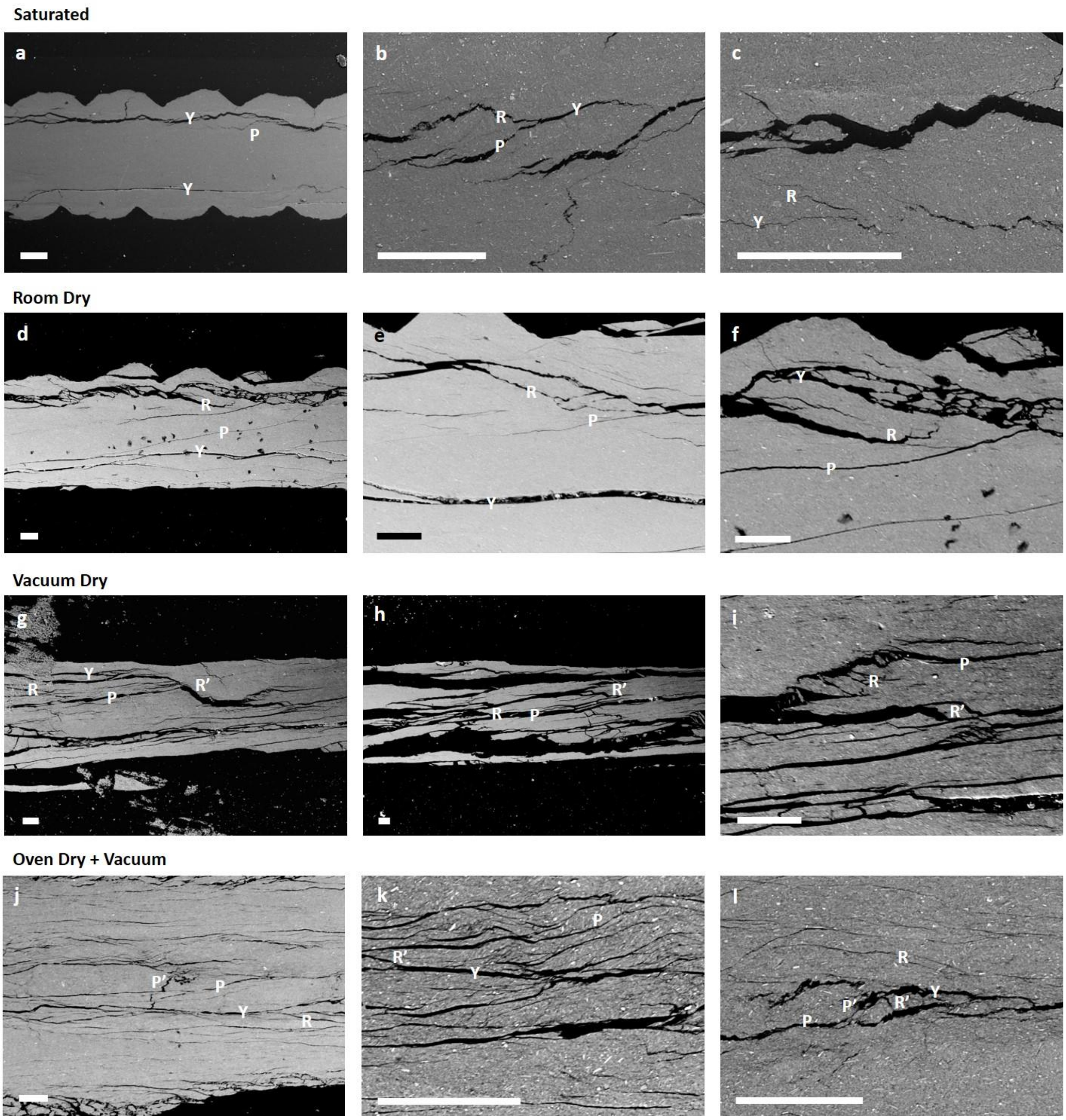
Saturated
a
Y
P
Y
b
R
Y
P
c
R
Y
Room Dry
d
R
P
Y
e
R
P
Y
f
Y
R
P
Vacuum Dry
g
R
Y
P
R'
h
R'
R
P
i
P
R
R'
Oven Dry + Vacuum
j
P'
P
Y
R
k
P
R'
Y
l
R
P'
R'
Y
P

Figure 8

Table 1: Yield and steady state friction coefficient (μ) data for experiments on kaolinite-rich china clay and Mg-montmorillonite.

Sample ID	Sample Type	Experiment Type	μ (yield)	μ (SS)	Shear Stress (yield) (MPa)	Shear Stress (SS) (MPa)
KLSAT01	Kaolinite-rich china clay	Saturated	0.273	0.262	16.38	15.72
KLSAT02	Kaolinite-rich china clay	Saturated	0.272	0.255	16.32	15.3
KLSAT03	Kaolinite-rich china clay	Saturated	0.265	0.26	15.9	15.6
KLRH01	Kaolinite-rich china clay	Room Humidity	0.292	0.296	17.52	17.76
KLRH02	Kaolinite-rich china clay	Room Humidity	0.37	0.4	22.2	24
KLVD01	Kaolinite-rich china clay	Vacuum Dry	0.405	0.42	24.3	25.2
KLVD02	Kaolinite-rich china clay	Vacuum Dry	0.4	0.415	24	24.9
KLODX01	Kaolinite-rich china clay	Oven Dry, no vacuum	0.34	0.42	20.4	25.2
KLODX02	Kaolinite-rich china clay	Oven Dry, no vacuum	0.37	0.44	22.2	26.4
KLODV01	Kaolinite-rich china clay	Oven Dry + Vacuum	0.43	0.465	25.8	27.9
KLODV02	Kaolinite-rich china clay	Oven Dry + Vacuum	0.36	0.44	21.6	26.4
KLVH01	Kaolinite-rich china clay	Vacuum + Heated in Vessel	0.4	0.485	24	29.1
KLVH02	Kaolinite-rich china clay	Vacuum + Heated in Vessel	0.34	0.46	20.4	27.6
MMSAT01	Mg-Montmorillonite	Saturated	0.156	0.118	9.36	7.08
MMRH01	Mg-Montmorillonite	Room Humidity	0.17	0.19	10.2	11.4
MMVD01	Mg-Montmorillonite	Vacuum Dry	0.2	0.217	12	13.02
MMODX01	Mg-Montmorillonite	Oven Dry, No Vacuum	0.58	0.57	34.8	34.2
MMODV01	Mg-Montmorillonite	Oven Dry + Vacuum	0.54	0.57	32.4	34.2
MMVH01	Mg-Montmorillonite	Vacuum + Heated in Vessel	0.51	0.56	30.6	33.6

Supplementary Table 1: Rate & state friction data for kaolinite-rich china clay and Mg-montmorillonite. VS = Velocity Step. Refer to Table 1 for experiment and sample type. Data rows left blank were not included in subsequent analyses due to significant error in the modelling process.

Sample ID	VS	a	a error	b	b error	d_c	d_c error	a-b	a-b error
KLSAT01	1	6.70E-03	5.04E-04	2.65E-03	4.84E-04	1.79E-05	4.18E-06	4.06E-03	9.88E-04
KLSAT01	2	5.05E-03	1.96E-04	1.04E-03	1.77E-04	5.39E-05	2.12E-06	4.00E-03	3.72E-04
KLSAT01	3	5.36E-03	3.12E-04	2.76E-04	2.94E-04	2.90E-05	3.76E-06	5.08E-03	6.06E-04
KLSAT02	1	5.98E-03	3.48E-04	1.18E-03	3.37E-04	2.67E-05	6.64E-06	4.80E-03	6.85E-04
KLSAT02	2	5.09E-03	2.39E-04	4.32E-04	2.28E-04	3.67E-05	2.65E-06	4.66E-03	4.66E-04
KLSAT02	3								
KLSAT03	1	5.49E-03	2.03E-04	1.08E-03	1.94E-04	2.64E-05	6.33E-06	4.41E-03	3.97E-04
KLSAT03	2	5.97E-03	2.76E-04	1.17E-03	2.70E-04	2.09E-05	5.74E-06	4.80E-03	5.46E-04
KLSAT03	3	6.27E-03	2.73E-04	5.54E-04	2.64E-04	1.81E-05	4.32E-06	5.71E-03	5.38E-04
KLRD01	1	4.10E-03	2.43E-04	6.91E-04	2.33E-04	3.22E-05	4.23E-06	3.41E-03	4.76E-04
KLRD01	2	4.45E-03	2.38E-04	7.06E-04	2.24E-04	3.43E-05	3.76E-06	3.74E-03	4.62E-04
KLRD01	3	3.90E-03	4.89E-04	2.31E-04	4.64E-04	1.51E-05	3.45E-06	3.67E-03	9.53E-04
KLRD02	1	2.19E-03	1.76E-04	8.54E-04	1.68E-04	2.14E-05	5.77E-06	1.34E-03	3.45E-04
KLRD02	2	2.59E-03	2.20E-04	3.97E-04	2.15E-04	1.23E-05	2.31E-06	2.19E-03	4.35E-04
KLRD02	3								
KLVD01	1	1.76E-03	1.40E-04	2.19E-04	1.35E-04	2.49E-05	9.03E-06	1.54E-03	2.75E-04
KLVD01	2	2.23E-03	6.08E-05	6.40E-05	1.76E-05	1.87E-05	5.51E-06	2.16E-03	7.84E-05
KLVD01	3								
KLVD02	1	1.71E-03	1.33E-04	6.26E-04	1.28E-04	2.35E-05	6.71E-06	1.09E-03	2.61E-04
KLVD02	2	2.08E-03	1.79E-04	-4.77E-04	-1.71E-04	1.96E-05	4.41E-06	2.55E-03	7.19E-06
KLVD02	3								
KLODX01	1	4.47E-03	4.64E-04	1.21E-03	4.61E-04	3.57E-06	1.49E-06	1.09E-03	2.61E-04
KLODX01	2	3.79E-03	7.12E-05	1.04E-03	6.64E-05	3.86E-06	4.52E-07	2.75E-03	1.38E-04
KLODX01	3	3.59E-03	7.13E-05	-1.20E-04	-6.73E-06	4.38E-06	3.96E-07	3.71E-03	6.46E-05
KLODX02	1	1.48E-03	5.58E-05	-3.59E-04	-8.07E-05	1.04E-05	5.21E-06	1.84E-03	-2.49E-05

KLODX02	2								
KLODX02	3								
KLODV01	1	2.30E-03	6.79E-04	1.04E-03	2.75E-04	2.83E-06	2.77E-08	1.26E-03	9.54E-04
KLODV01	2	1.84E-03	1.75E-04	6.13E-04	1.71E-04	9.05E-06	3.97E-06	1.22E-03	3.46E-04
KLODV01	3	2.13E-03	2.32E-04	7.26E-04	2.29E-04	1.03E-05	4.26E-06	1.41E-03	4.60E-04
KLODV02	1								
KLODV02	2	6.44E-03	3.76E-04	7.22E-03	2.53E-04	8.98E-06	1.83E-06	2.85E-03	6.29E-04
KLODV02	3								
KLVH01	1								
KLVH01	2	8.47E-03	4.55E-04	7.22E-03	2.74E-04	8.06E-06	1.57E-06	1.24E-03	7.29E-04
KLVH01	3	5.41E-03	9.33E-04	2.36E-03	9.31E-04	2.86E-06	1.27E-06	3.06E-03	1.86E-03
KLVH02	1	3.77E-03	3.12E-04	2.56E-03	3.06E-04	6.56E-06	1.10E-06	1.22E-03	6.18E-04
KLVH02	2								
KLVH02	3	6.82E-03	8.28E-04	4.34E-03	4.77E-04	2.58E-06	9.21E-07	2.48E-03	1.30E-03
MMSAT01	1	3.20E-03	9.88E-05	-4.04E-04	-9.60E-05	2.71E-05	7.55E-06	3.60E-03	2.79E-06
MMSAT01	2	3.45E-03	6.24E-05	-1.02E-03	-5.79E-05	7.92E-05	6.86E-06	4.47E-03	4.58E-06
MMSAT01	3	2.78E-03	6.07E-05	-6.10E-04	-5.68E-05	6.21E-05	9.04E-06	3.39E-03	3.90E-06
MMRH01	1	6.22E-03	9.76E-05	-5.61E-04	-9.13E-05	5.52E-05	1.28E-05	6.78E-03	6.31E-06
MMRH01	2	7.27E-03	7.07E-05	5.87E-04	6.62E-05	9.51E-05	2.16E-05	6.68E-03	1.37E-04
MMRH01	3	6.76E-03	1.02E-04	1.49E-03	9.51E-05	5.95E-05	5.69E-06	5.26E-03	3.90E-06
MMVD01	1								
MMVD01	2	7.51E-03	6.21E-05	-4.15E-04	-7.39E-05	1.10E-04	4.17E-05	7.93E-03	-1.19E-05
MMVD01	3	7.31E-03	1.39E-04	1.05E-03	1.30E-04	6.90E-05	1.92E-05	6.25E-03	2.69E-04
MMODX01	1	6.31E-03	6.51E-04	1.44E-03	8.44E-04	7.33E-06	5.49E-06	4.86E-03	1.11E-03
MMODX01	2	5.90E-03	6.02E-04	2.16E-03	5.90E-04	4.37E-06	1.39E-06	3.74E-03	1.19E-03
MMODX01	3								
MMODV01	1	8.52E-03	3.51E-05	5.35E-03	1.14E-03	1.25E-06	9.13E-07	3.17E-03	1.17E-03
MMODV01	2	7.49E-03	3.42E-04	2.65E-03	6.66E-04	2.76E-06	1.47E-06	4.84E-03	1.01E-03
MMODV01	3								
MMVH01	1								
MMVH01	2	6.17E-03	5.99E-04	3.61E-03	5.71E-04	7.75E-06	1.87E-06	2.57E-03	1.17E-03
MMVH01	3	8.19E-03	6.76E-04	3.73E-03	4.62E-04	6.34E-06	1.55E-06	4.46E-03	1.14E-03

Supplementary Material

Sample Equilibration Time Modelling

A fluid diffusion model (based on Faulkner et al. (2017)) was used to calculate pore fluid pressure equilibration times. For kaolinite, at minimal confining pressures, assuming a sample thickness of 1mm, an initial permeability of ~$10^{-19}$$\mathrm{m}^2$ (as measured in this study using the pulse-transient method), porosity of 20% (an approximate porosity of 100% clay that has experienced a small amount of confining pressure or shear strain estimated from Crawford et al. (2008) and Faulkner & Rutter (2000)), deionised water viscosity of $2.5\mathrm{x}10^{-5}$Pa.s (Likhachev, 2003) and compressibility of $4.5\mathrm{x}10^{-4}$$\mathrm{MPa}^{-1}$ (Kell, 1975), an equilibration time of ~0.5 to 1 hours was deemed sufficient. For Mg-montmorillonite, this was increased to >20 hours due to lower permeabilities (~$10^{-20}$$\mathrm{m}^2$ (to 10^{-22})m^2 (Behnsen & Faulkner, 2013; C. A. Morrow et al., 2017; this study)), particularly once water promotes clay swelling (Aksu et al., 2015). This step was deemed important, since if pore-fluid pressure is not given sufficient time to equilibrate (drain), gouge can appear falsely stronger, particularly in the early stages of an experiment, and velocity-strengthening behaviour can appear velocity-weakening (Moore and Lockner, 2011; Faulkner et al., 2018).

The time required for equilibration of a vacuum in clay samples was estimated using the same model (e.g. kaolinite, Supplementary Figure 1). Parameters used were the same as those used to estimate water saturation time, except substituting air viscosity for water viscosity ($1.98\mathrm{x}10^{-5}$Pa.s) and air compressibility for water compressibility (10 MPa^{-1}).

Supplementary Figure Captions

Supplementary Figure 1: Modelled simulation of the time taken to equilibrate a vacuum across a ~1 mm thick kaolinite-rich gouge sample. Each time step represents ~2 minutes. See Supplementary Material text for parameters used.

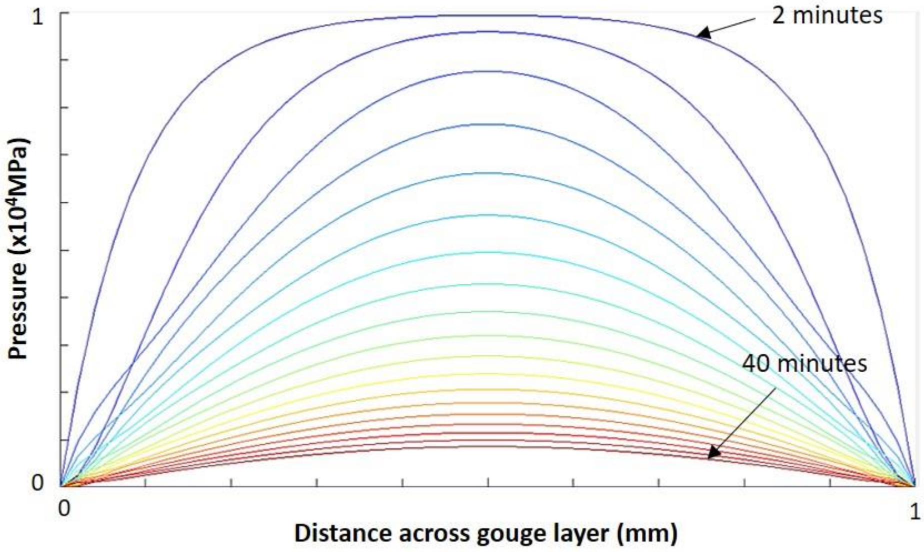

Supplementary Figure 1